Changes in relative humidity profiles over Earth's oceans in a warming climate: a satellite data based inference

Carsten Abraham[a,b] , Colin Goldblatt[b]

[a] *Canadian Centre for Climate Modelling and Analysis, Environment and Climate Change Canada, Victoria, British Columbia, Canada*

[b] *School of Earth and Ocean Sciences, University of Victoria, Victoria, British Columbia, Canada*

Corresponding author: Carsten Abraham, Carsten.Abraham@ec.gc.ca

Early Online Release: This preliminary version has been accepted for publication in *Journal of the Atmospheric Sciences*, may be fully cited, and has been assigned DOI 10.1175/JAS-D-22-0119.1. The final typeset copyedited article will replace the EOR at the above DOI when it is published.

ABSTRACT: Recently we presented a classification of ‘primitive’ relative humidity (RH) profiles into 8 distinct clusters over Earth’s oceans, based on about 18 years (2003-2020) of observations from the AIRS on NASA’s Aqua satellite. Here we investigate the seasonal variability and decadal trends, both in the vertical structure of these profiles, and in their associated area of occurrence. Since vertical structures (except in the marine boundary layer) of each RH-class are generally robust across all seasons and change only weakly in a warming climate, seasonal or decadal changes to their occurrence areas shift patterns of global moisture distribution. Globally, the marine boundary layer exhibits non-linear moistening effects after about 2010, the end of the warming hiatus. Annual timeseries of ocean areas dominated by RH-classes have linear trends, which are positive only for the most moist and driest RH-classes (in terms of the free troposphere) associated with deep convection and large-scale subsidence favouring conditions for low-level stratocumulus clouds, respectively. Based on estimated linear trends of RH-class occurrences and sea-surface temperatures, we infer projected linear responses of RH in a warming climate. Ocean areas dominated by most moist and driest RH-classes (in terms of the free atmosphere) are estimated to increase by about 1 and 2 %, respectively (corresponding to about 2.5 % K^{-1} and 4.5 % K^{-1}, respectively). The averaged global and tropical RH-structure remain almost constant in a warming climate. While this is consistent with other studies, our results show how increases in most moist and dry areas compensate each other, indicating possible increases in the frequency or persistence of future extreme events.

1. Introduction

Over Earth's oceans, atmospheric temperature profiles are relatively robust and similar across a wide range of underlying sea-surface temperatures (SST, Abraham and Goldblatt 2022). Consequently, atmospheric moistening processes, or changing atmospheric water vapour amounts in a warming climate, have to manifest themselves in systematic changes of relative humidity profiles (RH-profile). Climatologically, RH-profiles are observed to exhibit relatively robust structures (e.g Jordan 1958; Manabe and Wetherald 1967; Liu et al. 1991; Dunion 2011; Abraham and Goldblatt 2022). Abraham and Goldblatt (2022) showed through k-means clustering analysis that observed RH-profiles over Earth's oceans can be clustered into distinct 'primitive' classes: 6 for clear-sky and 8 for all-sky conditions. These classes were found to not only have distinct structural features associated with particular large-scale atmospheric dynamics but also to have particular effects on the spatial structures of large-scale outgoing longwave radiation (OLR). Changes to atmospheric water vapour distributions and corresponding OLR values are then simply reflected by changes to the occurrence probabilities (OP) of each RH-profile class. In this study we investigate, first, the seasonal variability of OPs and vertical structures of the distinct RH-profile classes; second, we estimate decadal changes of these properties to infer global RH-profile responses to a warming climate.

The analysis presented here focuses only on the timeseries of the 8 RH-profile classes for all-sky conditions (denoted here RH-classes A1 to A8). For clear-sky conditions we identified 6 distinct 'primitive' RH-profile structures which have a one-to-one correspondence to all-sky RH-profile structures (Abraham and Goldblatt 2022). Due to these close relationships between RH-profile structures for clear-sky and all-sky conditions we found no considerable differences to seasonal and decadal changes to OPs or RH-structures between corresponding RH-profile classes for clear-sky and all-sky conditions. A summary analysis for the 6 RH-profile classes for clear-sky conditions is provided in the supplementary material.

The launch of NASA's Aqua satellite equipped with the hyperspectral Atmospheric Infrared Sounder (AIRS) in 2002 marked a new beginning for observing atmospheric water vapour content above Earth's oceans (Aumann et al. 2003; Kalmus et al. 2015). Historically, RH-profiles above Earth's oceans were estimated from coastal radiosonde ascents as systematic measurements above the oceans were unfeasible (e.g. Jordan 1958; Manabe and Wetherald 1967; Liu et al. 1991;

Dunion 2011). Despite the geographical limitations, those studies identified similar RH-profile structures across different coastal regions. Using latitudinal averages Ruzmaikin et al. (2014) confirmed on the basis of AIRS data that distinct vertical RH structures are particular to latitudinal bands. Systematic k-means RH-profile clustering of AIRS data further showed that not only the prevalent atmospheric circulation in latitudinal bands determines RH-profile structures but also the underlying sea-surface temperatures (SST): Increasing SSTs promotes a moistening of the atmosphere, observable by large increases in OPs of most moist RH-profile classes accompanied by only weak increases to their RH magnitudes (Abraham and Goldblatt 2022).

Abraham and Goldblatt (2022) identified 8 different typical RH-profile structures for all-sky conditions, A1–A8. Characteristics, vertical structures, and particular features of the distinct classes are summarized and depicted in Fig. 1. In contrast to Abraham and Goldblatt (2022), climatological values of a state variable X (e.g., SST) associated with each RH-profile class (Fig. 1; rows 7 and 8) are not calculated as an average over the classified data set but from a weighted-average accounting for the relative importance of a RH-profile class, k with $k \in \{\mathrm{A1}, \mathrm{A2}, \ldots, \mathrm{A8}\}$, in dominating a particular region. For X we estimate k-conditioned climatological means, $\overline{X(k)}$ (overbars denote climatological means), with

$$\overline{X(k)} = \sum_{\phi,\lambda} w_k(\phi,\lambda)\ \overline{X(k,\phi,\lambda)}, \tag{1}$$

where

$$w_k(\phi,\lambda) = \frac{\overline{\mathrm{OP}(k|\phi,\lambda)}}{\sum_{\phi,\lambda}\overline{\mathrm{OP}(k|\phi,\lambda)}}, \tag{2}$$

where ϕ and λ denote the geographical latitude and longitude, respectively, and $\mathrm{OP}(k|\phi,\lambda)$ is the conditional OP of RH-profile class k on a uniform square degree latitude-longitude grid. Bootstrapping analyses (1000 samples) show almost no variability (variance is several orders of magnitude smaller) around climatological values (not shown). Increasing the resolution of the grid does not change the estimates substantially.

Of the 8 different RH-profile classes four are particular to the tropics (A1–A4), and two to the subtropics (A4–A5). Remaining classes A6–A8 are particular to mid- and high-latitudes. While all mean profiles share moist marine atmospheric boundary layers, vertical RH-structures differ substantially in the free troposphere.

Tropical profiles stand out through narrow RH-peaks near the tropopause consistent with findings in earlier studies (e.g. Ovarlez et al. 2002; Ström et al. 2003; Ruzmaikin et al. 2014). The inner-tropical convergence zone (ITCZ) and the Indo-Pacific warm pool, regions with warm SSTs, are associated with the most-moist RH-profiles A1 and A2 consistent with the dynamics of deep convection (Abraham and Goldblatt 2022). Those classes can be associated with total column water vapour (TPW) amounts around $50\,\mathrm{kg\,m^{-2}}$ (Fig. 1; row 8) causing substantial attenuation of OLR and the super-greenhouse effect (SGE, Abraham and Goldblatt 2022).

All other RH-profile classes are associated with substantially lower TPW abundances and cannot be associated with the SGE. Class A3, characterized by a "C-shape" vertical RH distribution, occurs most often within the tropics outside the ITCZ. While all tropical RH-profiles exhibit features of vertical RH-structures establishing in radiative-convective equilibrium (RCE, Romps 2014), the "C-shape" form of A3 is the most similar to the theoretical profiles in RCE. Such "C-shape" RH-profile structures form when vertical gradients in water vapour lapse rate are largest in altitudes where large-scale subsidence exceeds convection (Romps 2014). The RH-peak of A4 near the top of the atmospheric boundary layer in combination with the dry free-troposphere and its unique occurrence in cloudy conditions allows for associating this class with low-level stratocumulus clouds (Abraham and Goldblatt 2022). This class occurs mainly in the trade wind regions. The dry conditions in the upper troposphere of A4–A5, particular to the subtropics, are caused by eddy motions along isentropes transporting moisture into the mid-latitudes where they dehydrate before returning to the subtropics (Galewsky et al. 2005).

The characterization of distinct robust climatological RH-profile structures, as conducted in Abraham and Goldblatt (2022), is important, for instance, to study climate sensitivities in RCE model frameworks (e.g Manabe and Wetherald 1967; Augustsson and Ramanathan 1977; Satoh and Hayashi 1992; Rennó et al. 1994; Dacie et al. 2019; Kluft et al. 2019; Bourdin et al. 2021) or to understand the stability of climate to water vapour feedback (Goldblatt et al. 2013; Dewey and Goldblatt 2018). Understanding further whether a warming climate causes systematic changes to those RH-profile classes or simple changes to their OPs allows further characterization of atmospheric water vapour feedbacks. In this study we determine how OPs and RH structures of distinct RH-classes have developed over the 18 years of observations in order to infer RH feedbacks

Accepted for publication in *Journal of the Atmospheric Sciences*. DOI 10.1175/JAS-D-22-0119.1.

RH-profile class	A1	A2	A3	A4	A5	A6	A7	A8
	Moist		⟶		Dry	⟶		Moist
Region	Tropics			Tropics, Subtropics	Subtropics	Mid-latitudes		High-latitudes
Structure ▬ All ▬ DJF ▬ MAM ▬ JJA ▬ SON	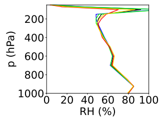	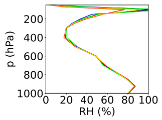	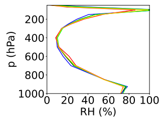	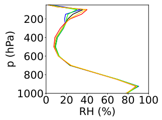	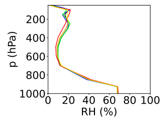	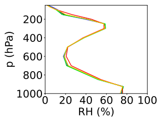	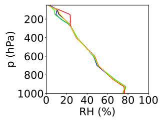	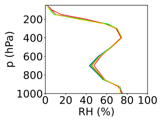
Main characteristics of vertical RH-structure in the troposphere	almost constant RH-values (around 60 %); RH-peak near tropo-pause	linear decrease from 80 % at 925 hPa to 20 % at 200 hPa; RH-peak near tropo-pause	"C-shape" (Romps 2014); RH–peak near tropopause	boundary-layer top around 100 % RH, dry tropo-sphere (RH < 20%)	constant dry troposphere (RH < 15 %)	moist upper tropo-sphere with a dry middle troposphere	linear decrease similar to profiles in Manabe and Wetherald (1967)	large RH-values (RH > 50 %) in the whole troposphere
Associated dynamics	deep convection		height variations in the water vapour lapse rate due to large-scale subsidence exceeding convective activity (Romps 2014)		mid-latitude eddies transporting moisture along isentropes from subtropics into the mid-latitudes where they dehydrate before returning into the subtropics (Galewsky et al. 2005)			
Special features	strong	weak		low-level strato-cumulus cloud-decks	mainly clear-sky conditions			
$\overline{f_{\text{ocean}}}$ (%)	9.31	9.57	8.78	14.14	14.63	15.61	14.60	13.36
$\overline{\text{SST}}$ (K)	301.1	300.6	299.9	292.0	290.4	284.7	281.6	276.1
$\overline{\text{TPW}}$ (kg m^{-2})	52.5	48.4	32.9	23.6	15.2	15.7	16.3	11.2

FIG. 1. Summary of the characteristics of the 8 distinct RH-profile classes for all-sky conditions as determined in Abraham and Goldblatt (2022) including dominant occurrence regions, main features of the vertical RH-structures, atmospheric dynamics that can be associated with the distinct classes. Finally, the associated climatological ocean area fraction dominated by a RH-profile class ($\overline{f_{\text{ocean}}}$), mean sea-surface temperatures ($\overline{\text{SST}}$), and mean total column water vapour amounts ($\overline{\text{TPW}}$) are provided. In contrast to Abraham and Goldblatt (2022), presented climatological means of SST and TPW take into account the non-uniform distribution of observations across the globe according to Eqs. 1, and 2.

Accepted for publication in *Journal of the Atmospheric Sciences*. DOI 10.1175/JAS-D-22-0119.1.

to a warming climate. In order to retrieve robust estimates of the inferred response to a warming climate we investigate seasonal variability which will then be accounted for.

We first revise the data used (Sec. 2) before presenting results of the seasonal variability to RH-profile structures and OPs as well as inferred responses to a warming climate in Sec. 3; conclusions are given in Sec. 4.

2. Data and Methods

In Abraham and Goldblatt (2022) we clustered instantaneous satellite observations (about 450 million) of atmospheric RH-profiles above Earth's oceans into distinct 'primitive' classes. Those RH-profiles were retrieved from the AIRS on NASA's Aqua satellite between August 30 2002 and March 6 2021 (Kalmus et al. 2015). The RH-profiles are directly provided in the AIRS Version 7 Level 2 product and are derived from the retrieved profiles of water vapour mixing ratios and temperature-dependent water vapour saturation mixing ratios relative to the stable phase of water, i.e. saturation mixing ratios relative to the liquid and ice phase of water. Accounting for the stable phase of water vapour often causes relative humidity in ice-clouds and freezing layers to exceed saturation values (Ovarlez et al. 2002; Ström et al. 2003; Korolev and Isaac 2006). This supersaturation is often observed in the upper tropical troposphere (Abraham and Goldblatt 2022).

The AIRS Version 7 Level 2 product provides the RH-values on 14 standard pressure levels (p) between 1000 hPa and 50 hPa (1000, 925, 850, 700, 600, 500, 400, 300, 250, 200, 150, 100, 70, and 50 hPa) such that the vertical resolution is about 3 km (Maddy and Barnet 2008). The footprint of the AIRS retrievals is ~ 45 km. Here, we investigate satellite retrievals of both day-time and night-time overpasses. As shown in Abraham and Goldblatt (2022) differences in both RH-structures and OP of RH-profile classes are small allowing for this simplification. Furthermore, we make use of estimates under all-sky conditions of the SST, OLR, and TPW, as well as metdata about the time and geographic location (Table 1). A more detailed description of the data is provided in Abraham and Goldblatt (2022).

As in Abraham and Goldblatt (2022), we use only data with good quality flags (AIRS QF ≤ 1; Susskind et al. 2003, 2006). We require this quality flag requisite for both moisture and temperature measurements on each of the 14 pressure levels, as well as for SST, OLR, TPW, and total cloud cover retrievals as we study properties of the whole atmospheric column. The moisture estimates

Table 1. Top: Variables, their acronyms used throughout the paper, and corresponding product variable names of the hyperspectral Atmospheric Infrared Sounder (AIRS) on NASA's Aqua satellite. All data is taken for all-sky conditions. Bottom: metadata used from AIRS are listed.

Variable	Acronym	AIRS variable name
Sea-surface temperature	SST	TSurfStd
Outgoing longwave radiation	OLR	olr
Total precipitable water vapor	TPW	totH2OStd
Relative humidity profiles	RH-profiles	RelHum
Metadata		
Date and time		
Latitude		
Longitude		
Surface class		

with these AIRS QFs are accurate within 15 ppm and 6 ppm below and above 300 hPa, respectively (Divakarla et al. 2006; Trent et al. 2019). The T-profiles with AIRS QF ≤ 1 are accurate within ± 0.5 K compared to in-situ measurements (Divakarla et al. 2006; Diao et al. 2013; Feltz et al. 2017); SST measurements have standard errors lower than 1.4 K (Nalli and Smith 2003; Susskind et al. 2003).

The hyperspectral averaging kernels for water vapor are typically largest (hence making retrievals most accurate) between 800 and 250 hPa; conversely the averaging kernels are smallest (and hence retrievals least accurate) in the planetary boundary layer (surface to about 800 hPa) and upper troposphere or lower stratospehre (above 200 hPa). This design choice ensures RH biases in the lower and mid-troposphere to be generally much smaller than 10 % (Gettelman et al. 2004; Divakarla et al. 2006; Susskind et al. 2006; Pu and Zhang 2010, e.g.); RH biases in the upper troposphere and lower stratosphere, however, increase substantially. Across several geographical locations, RH values of AIRS in atmospheric levels of the upper troposphere and lower stratosphere have been validated against in-situ measurements from radiosonde measurements and profile flights from aircraft. The AIRS biases of RH in the upper troposphere and stratosphere are generally between 20 % and 50 % when AIRS QF ≤ 1 (e.g. Gettelman et al. 2004, 2006; Diao et al. 2013; Osei et al. 2020). As shown in Abraham and Goldblatt (2022), RH-profile classes particular to the tropics exhibit often supersaturated conditions of about 20-50 % in those regions. These values are

Accepted for publication in *Journal of the Atmospheric Sciences*. DOI 10.1175/JAS-D-22-0119.1.

related to the fact that RH is estimated over the stable phase of water (ice phase in these conditions) which are often observed to be supersaturated (Ovarlez et al. 2002; Ström et al. 2003; Korolev and Isaac 2006). While those RH values can be substantially overestimated, as mentioned above (since AIRS is designed to measure the middle tropospheric water vapour content with high accuracy at the expense of accuracy in the boundary layer and upper troposphere), an increase of water vapour toward an RH peak near the tropopause is observed in RH estimates over both the liquid and ice phase (Sandor et al. 2000; Takahashi et al. 2016; Kluft et al. 2019). The RH over the liquid phase remains typically below saturation in the upper troposphere and lower stratosphere while the RH-peak over the ice-phase is often supersaturated.

The near-surface moisture measurements (around the 1000 hPa) are typically dry biased by about 10-20 % (Divakarla et al. 2006; Pu and Zhang 2010) and are therefore not discussed in detail in this study. At 925 hPa, a height usually still within the marine boundary layer, moisture biases, however, decrease substantially (Pu and Zhang 2010). Furthermore, vertical water vapour gradients within the marine boundary layer from AIRS are consistent with in-situ measurements and other satellite products (Stevens et al. 2003).

Atmospheric profiles are estimated from cloud-cleared AIRS radiances (Chaine et al. 2006). Poorest retrievals are associated with largest amounts of water vapour in the atmospheric column consistent with large precipitation rates (Kahn and Teixeira 2009). Furthermore, the cloud-clearing algorithms of the AIRS product perform better in the presence of a mixture of cloud and clear-sky conditions across the observational domain as it allows for larger contrasts of radiative retrievals and more accurate estimates of clear-sky radiances. Thus, areas which have relatively uniform radiative fluxes, i.e. stratocumulus cloud decks or no clouds at all, also result in unreliable RH-profile estimates. For that reason the AIRS QF applied here skews data towards clear-sky and mixed conditions, resulting in a heterogeneous global data coverage (Figure 2).

The geographical distribution of the data (with the AIRS QF ≤ 1 applied for all variables) is, nonetheless, approximately symmetric across both hemispheres with an almost uniform distribution between 40 N and 40 S, except from areas often covered by stratocumulus cloud decks (west of North and South America, and Southern Africa). Substantially fewer measurements are available north and south of 40 N and 40 S, respectively due to the effects discussed above. Overall, the stringent AIRS quality flag requirements filter about two thirds of all data. Since the Aqua satellite

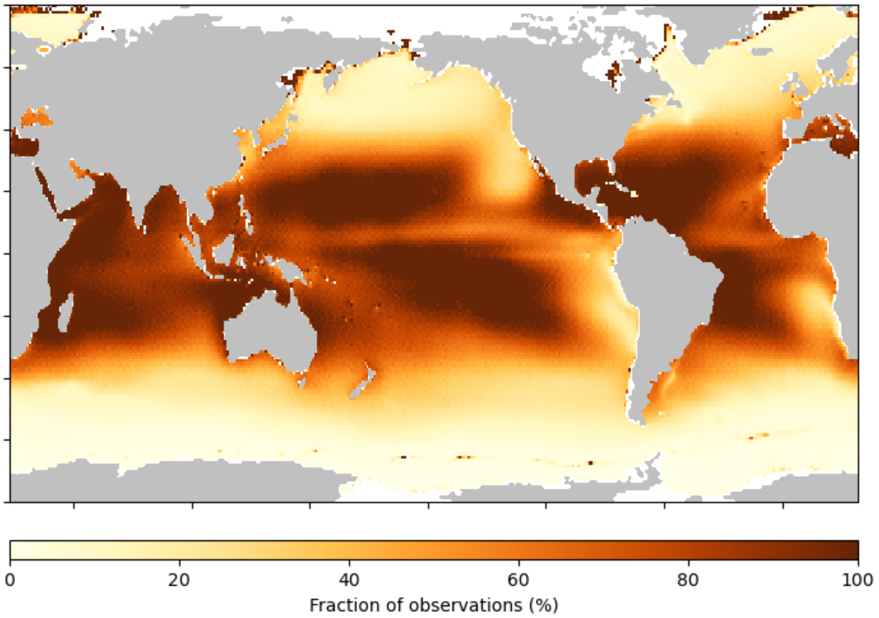

Fig. 2. Fraction of observed data with an AIRS QF ≤ 1 (as used throughout this analysis) on a square degree rectangular longitude latitude grid.

is polar orbiting (hence more high-latitude than tropical measurements are taken), our data quality requirements clearly filter disproportionately mid- to high-latitude measurements while only few data are filtered in the tropics and subtropics. While this might have caused not capturing all RH-profile classes in mid- to high-latitudes, the RH-profile structures derived are neither particularly wet nor dry and are close to climatological mean RH-values (cf. RH-profiles of A6–A8 in Fig. 1, row 3, with Ruzmaikin et al. 2014). Therefore, inferred warming responses on the global RH distribution are likely not substantially affected by the filtering.

We account for the spatial variability of data distribution imposed by our AIRS QF requirements by estimating from conditional OPs on a square degree uniform latitude-longitude grid the areal ocean fraction, f_{ocean}, that is on average dominated by each of the 8 RH-profile classes. At each grid point we estimate from 100 bootstrapping samples the mean conditional OP of each RH-profile class, $\text{OP}(k|\phi,\lambda)$ with $k \in \{\text{A1}, \text{A2}, \ldots, \text{A8}\}$. The $\text{OP}(k|\phi,\lambda)$ are not sensitive to a higher grid resolution. The $f_{\text{ocean}}(k)$ is then given by

$$f_{\text{ocean}}(k) = \sum_{\phi,\lambda} \frac{A(\phi,\lambda)}{A_{\text{ice-free-ocean}}} \text{OP}(k|\phi,\lambda), \tag{3}$$

where $A(\phi,\lambda)$ is the grid-area centred at latitude ϕ and longitude λ, and $A_{\text{ice-free-ocean}}$ the global ice-free ocean area. Similarly, we calculate global mean values of other state variables $\langle X \rangle$ (e.g., X is SST, OLR, or TPW):

$$\langle X \rangle = \sum_{\phi,\lambda} \frac{A(\phi,\lambda)}{A_{\text{ice-free-ocean}}} \overline{\mathrm{X}(\phi,\lambda)}. \tag{4}$$

We use $\langle \cdot \rangle$ to denote global averages.

In order to estimate decadal trends from any timeseries of a state variable, X_t, we remove from monthly means the seasonal cycle, X_s, to create seasonal stationary timeseries $X_t - X_s$. X_s is derived by fitting a sum of sine and cosine functions to X_t using 4 frequencies (n):

$$X_s = \sum_{n=1}^{4} c_n \sin(n\omega t) + d_n \cos(n\omega t), \tag{5}$$

where $\omega = \frac{2\pi}{12}$, and c_n, d_n are fitted amplitudes of each frequency. Finally, trends are estimated through linear-fits to $X_t - X_s$. Both fits are performed with the linear least-squares method.

Based on k-means cluster analysis, we classified the satellite retrieved RH-profiles for all sky-conditions into 8 distinct classes (A1–A8, Abraham and Goldblatt 2022). The retrieved cluster affiliation of each RH-profile observation, together with time and location information, is used in this study to investigate the seasonal variability to the vertical RH-structures, RH-class occurrences, and their decadal trends.

3. Results

a. Seasonal Cycle

1) RH-STRUCTURES

Seasonal variations to the mean vertical structures in each RH-profile class are small (Fig. 1; row 3). Some changes are only evident for the RH-peak near the tropopause in tropical classes A1–A3. In winter and spring (DJF and MAM, respectively) the RH-peak is more pronounced than in summer and fall (JJA and SON, respectively). This change is related to the fact that RH-peaks near the tropical tropopause are more pronounced in the Southern Hemisphere than in the Northern Hemisphere (Abraham and Goldblatt 2022). As A1 and A2 occur within the ITCZ, the RH-peak changes near the tropopause reflect simply latitudinal shifts of the ITCZ towards the

Southern Hemisphere in DJF and MAM. However, this is also the altitude range in which AIRS measurements are least accurate. Nonetheless, the RH-peak near the tropopause in the tropics remains a robust feature across all seasons.

The RH-profile distributions around the means are symmetric and relatively narrow (not shown), similar to the annual distributions discussed in Abraham and Goldblatt (2022). That vertical structures of the distinct RH-profile classes remain almost the same over the course of the year indicates, first, how robust features of the distinct RH-structures are and, second, that seasonal changes to the climatology of atmospheric water vapour abundance have to manifest themselves primarily in changes to $f_{\text{ocean}}(k)$.

2) Occurrence probabilities

On average, over the about 18 years of observations ocean fractions dominated by each class are relative similar (Fig. 1; row 6). About 20 % of Earth's oceans are dominated by profiles associated with deep-convective activity and consequently moist conditions (A1 and A2). In contrast, about 35 % of Earth's oceans are dominated by drier conditions in the free atmosphere (A3–A5).

In this data set, monthly mean values of f_{ocean} of all RH-profile classes exhibit seasonal cycles with predominantly annual and semiannual harmonics, yet amplitudes are generally largest for tropical and subtropical classes (A2–A4; Fig. 3, column 1). The f_{ocean} of most extratropical classes exhibit weaker seasonal amplitudes, except for A7. The f_{ocean} of all classes exhibit a regular seasonal cycle without any phase shifts and only weak interannual variability. Our discussion in this section begins with the tropical and sub-tropical classes (A1–A5), followed by the mid- to high-latitudes (A6–A8).

The annual cycle of $f_{\text{ocean}}(\text{A1})$ oscillates between January minima of about 8 % and September maxima of about 13 % (Fig. 3). By contrast, $f_{\text{ocean}}(\text{A2})$ shows semiannual harmonics with maxima in April and October–November and minima in January and July, hence lagging behind the equinoxes and solstices, respectively, by about a month. Even though the signal is weak, semiannual harmonics are also present in the $\langle\text{SST}\rangle$, with minima and maxima preceding the minima and maxima of $f_{\text{ocean}}(\text{A2})$ by about a month (Fig. 4; row 1).

The annual cycles of $\langle\text{TPW}\rangle$ exhibit two local maxima (March–April and September), generally in agreement with f_{ocean} of classes A1 and A2 (cf. Figs. 3 and 4). Profiles A1 and A2 hold 2 to 3

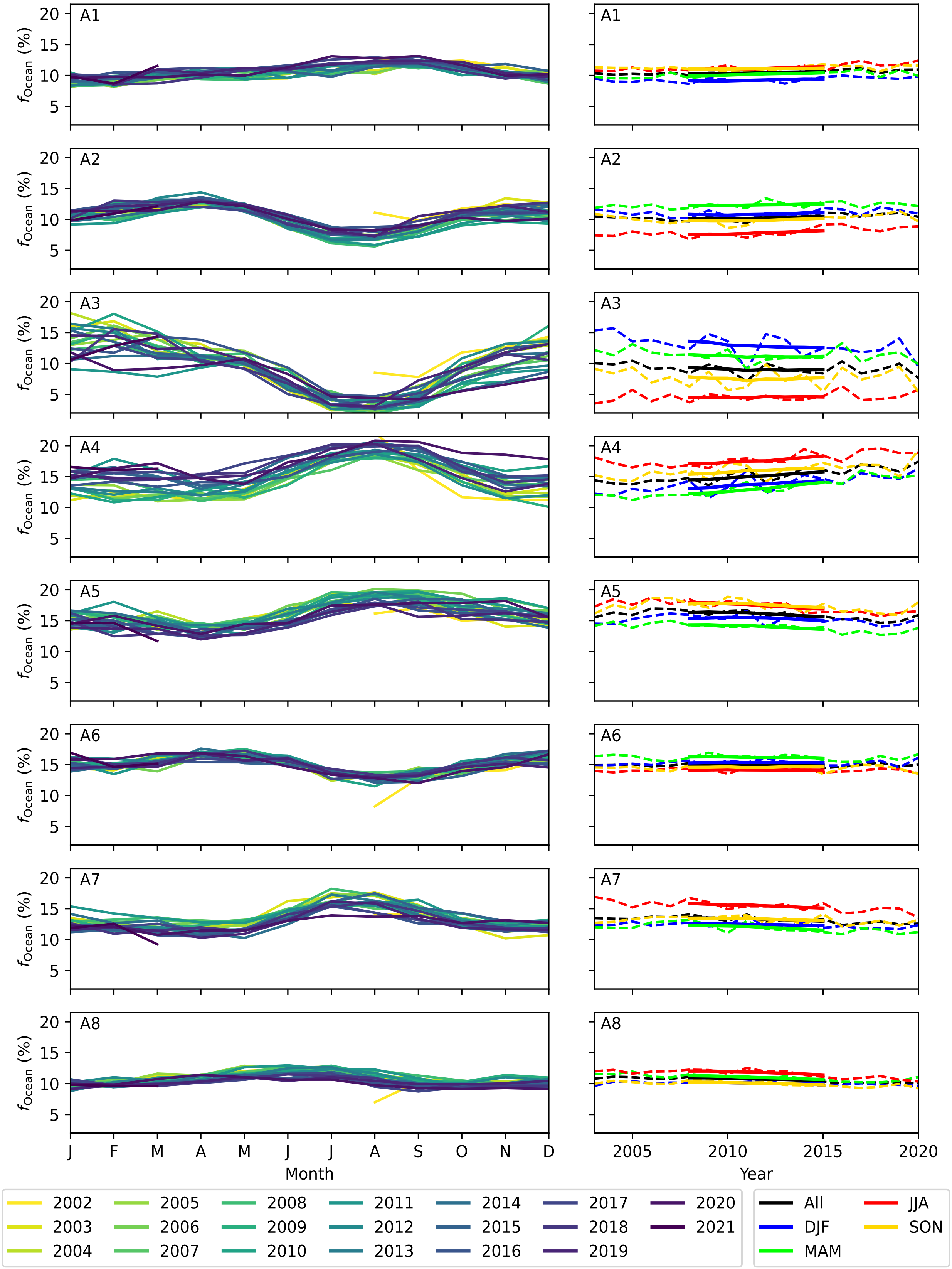

Accepted for publication in *Journal of the Atmospheric Sciences*. DOI 10.1175/JAS-D-22-0119.1.

FIG. 3. Column 1: Annual cycles (2002-2021) of monthly mean ice-free ocean fractions (f_{ocean}) that are dominated by each RH-profile class (rows). The f_{ocean} values sum up to 100 % in each month of every year. Column 2: Annual and seasonal mean f_{ocean} from 2003 to 2020 (dashed lines). Solid lines illustrate the 10-year moving averages.

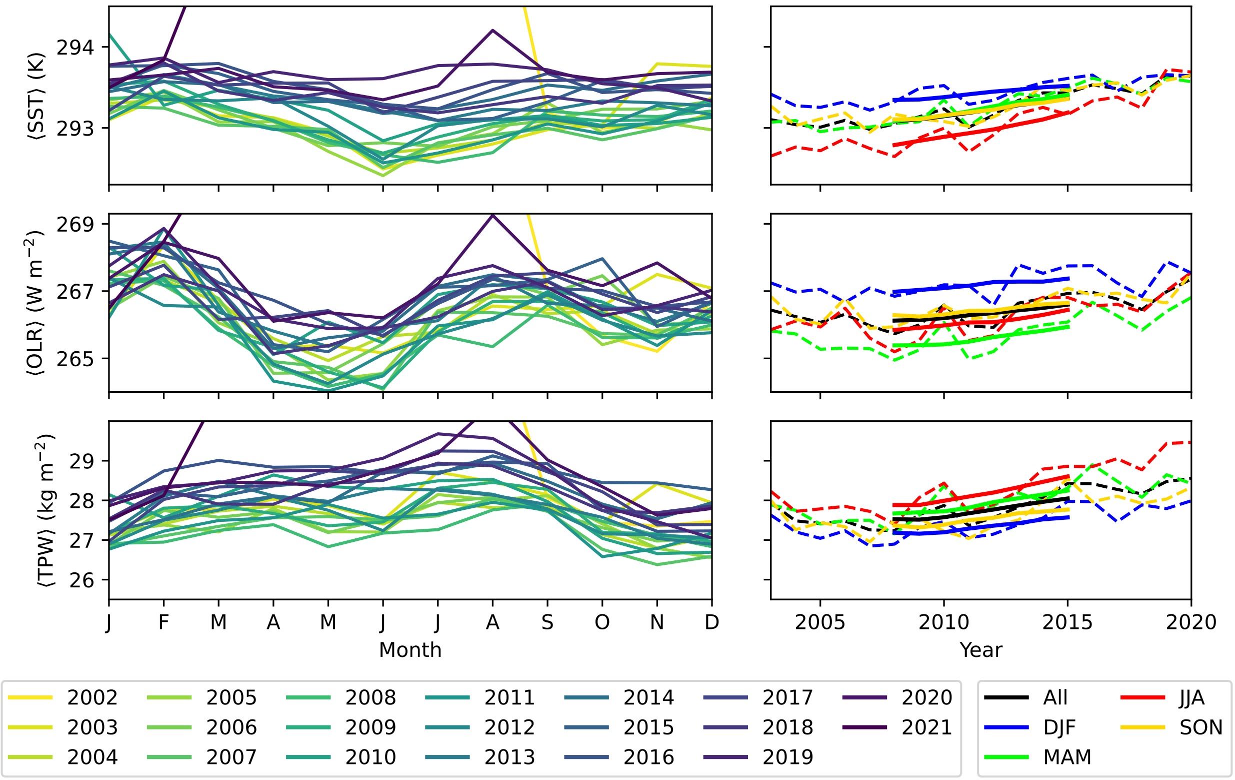

FIG. 4. Left: Annual cycle of the monthly globally averaged SSTs (row 1), OLR (row 2), and TPW (row 3) from 2003 to 2020 for all-sky conditions. Right: Annual and seasonal means (dashed) as well as the 10-year moving averages (solid).

times more TPW than all other classes (because of their association with deep convection, Fig.1; row 8), so the annual ⟨TPW⟩ cycle is a direct consequence of the annual cycles $f_{\text{ocean}}(\text{A1}, \text{A2})$. The asymmetry in the annual ⟨TPW⟩ cycle (a larger September peak) arises from superposition of f_{ocean} peaks in the annual cycles of A1 and A2.

The seasonal cycle of geographical regions dominated by A1 and A2, which are associated with stronger and weaker deep convection, correlate with the seasonal cycle of SST in the tropics (cf. Fig. 5 and Fig. 6); Abraham and Goldblatt (2022) demonstrated that A1 and A2 start to occur frequently for SST > 298 K and become the governing classes for SST > 301 K. Particularly the warming of Northern Hemisphere Indo-Pacific warm pool region and oceans around Middle America in JJA drive systematic increases of OPs of A1. Since oceans on the Southern hemisphere do not warm as much as the aforementioned Northern Hemisphere ones, the slightly colder SST drive the f_{ocean}(A2) maxima in MAM. The spatial OP patterns of classes A1 and A2 together are very similar to those of OLR minima and TPW maxima in each season (cf. Fig. 5 and Fig. 6).

There are some striking regional patterns in OPs of classes A1 and A2 (Fig. 5). The Indo-Pacific warm pool (East Indian Ocean, the Bay of Bengal, South China Sea, Philippine Sea), as well as oceans around Middle America exhibit a systematic warming from DJF to JJA, such that seasonal mean SSTs exceed 301 K (Fig. 6; column 1, dashed line). Consistently, in these regions a shift occurs from primarily dry conditions (associated with profile A3) in DJF, to primarily wet conditions (associated with profiles A1–A2) in JJA (Fig. 5). In some of those regions, OPs of A1 change from below 10 % in DJF to well above 90 % in JJA. In particular, the East Indian Ocean and the Bay of Bengal experience no other profile than A1 during JJA. Consistent with the fact that the tropical East Pacific and Atlantic Ocean have seasonal mean SSTs usually below 301 K those regions can be most often associated with weaker deep convection (A2).

Finally, the f_{ocean} of RH-profile classes A1 and A2 do not appear to be strongly correlated (Fig. 7), suggesting that no coupling through atmospheric dynamics between these two classes exist. Instead, profile A1 simply replaces A2 with increasing SST.

RH-profiles A3–A5 occur mainly in the tropics to subtropics, all involving large-scale subsidence (Fig. 1). The seasonal amplitudes of f_{ocean} cycles of A3 and A4 are large, while that of A5 is smaller (Fig 3), but all exhibit evident correlations with the f_{ocean} of A1 and A2 (Fig. 7).

The characteristics of profiles representing descending air depends on the strength of deep convection (Fig. 7). The f_{ocean}(A3) shows a substantial minimum in July–September which is well correlated ($r = 0.8$) with f_{ocean}(A2) minima (weaker deep convection) but anti-correlated ($r = -0.7$) with the f_{ocean}(A1) (strong deep convection). Conversely, the f_{ocean}(A4) maxima in July–September are positively correlated ($r = 0.62$) with f_{ocean}(A1) but anti-correlated ($r = -0.75$) with f_{ocean}(A2). Thus, we find that f_{ocean}(A3) (weak large-scale subsidence allowing some convective activity in the lower troposphere) is favoured when weak deep convection occurs, and

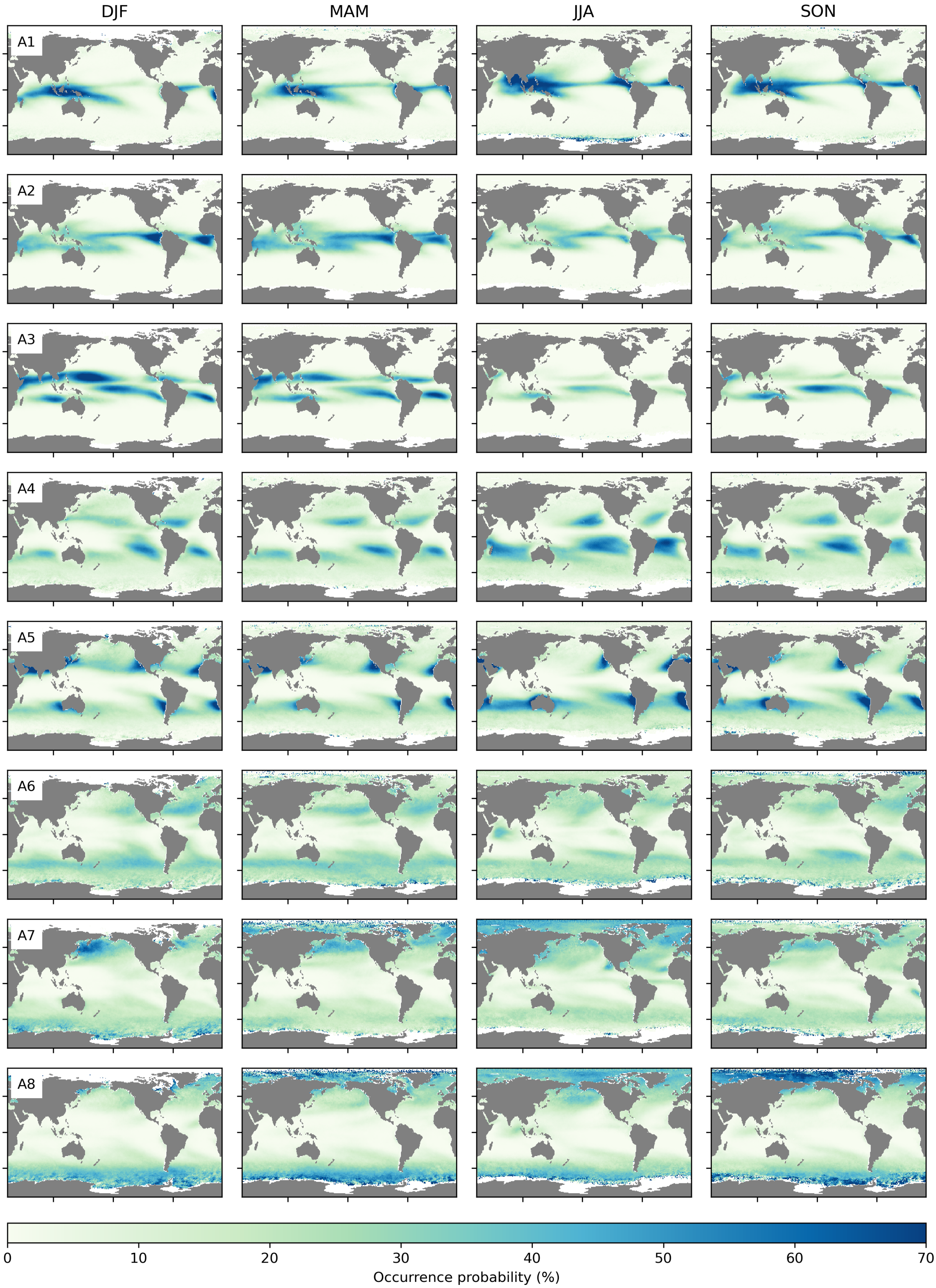

Accepted for publication in *Journal of the Atmospheric Sciences*. DOI 10.1175/JAS-D-22-0119.1.

Fig. 5. Seasonal (columns) occurrence probabilities of the 8 RH-profile classes (rows) on a 1 square degree uniform latitude-longitude grid. The annual averages of occurrence probabilities are illustrated in Abraham and Goldblatt (2022, Fig. 8, column 2).

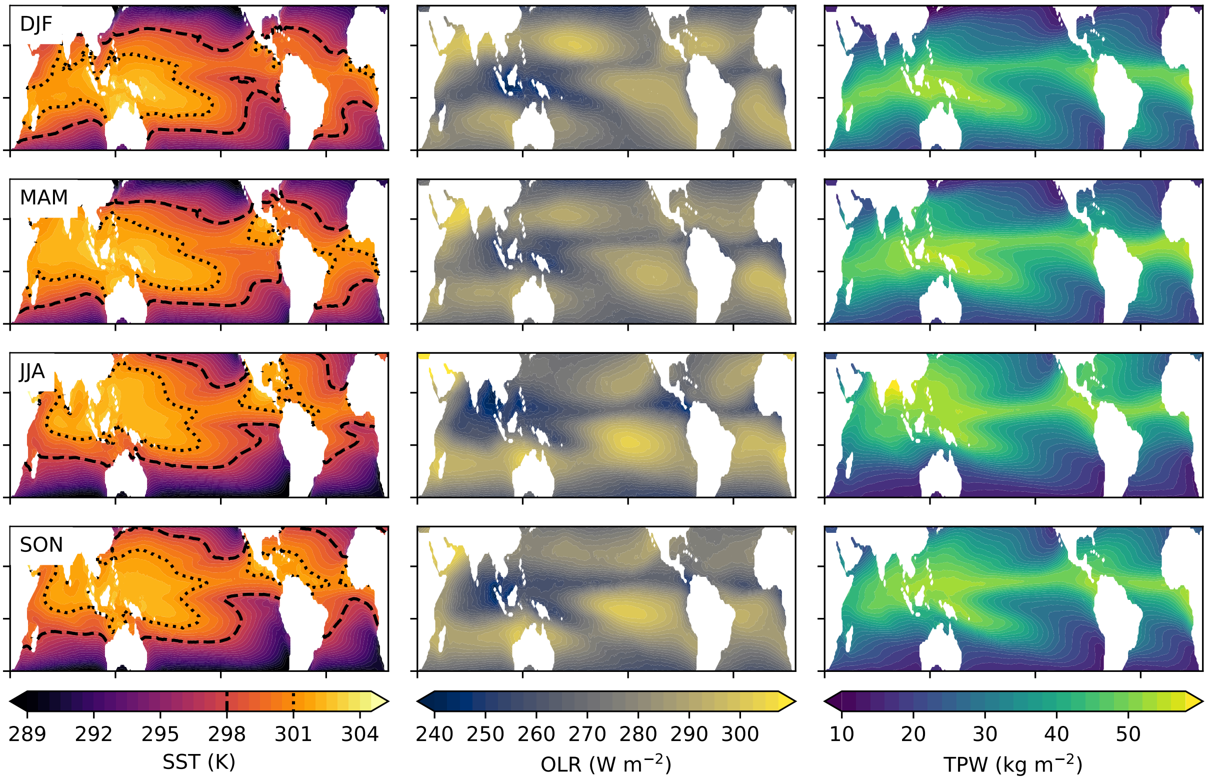

Fig. 6. Seasonal (rows) mean SST (column 1), OLR (column 2), and TPW (column 3) in the zonal band 35 N to 35 S between 2003 and 2020 for all-sky conditions. Dashed and dotted lines in column 1 illustrate SST isothermes of 298 K and 301 K, respectively.

f_{ocean}(A4) (strong large-scale subsidence suppressing convective activity and favouring low-level stratocumulus clouds) increases when strong deep convection is present. Consistently, f_{ocean} of A3 and A4 are anticorrelated.

Geographically, A3 and A4 occur most often in regions around the ITCZ and deep convection (Abraham and Goldblatt 2022). No particular region dominates the seasonal cycle (Fig. 5).

Accepted for publication in *Journal of the Atmospheric Sciences*. DOI 10.1175/JAS-D-22-0119.1.

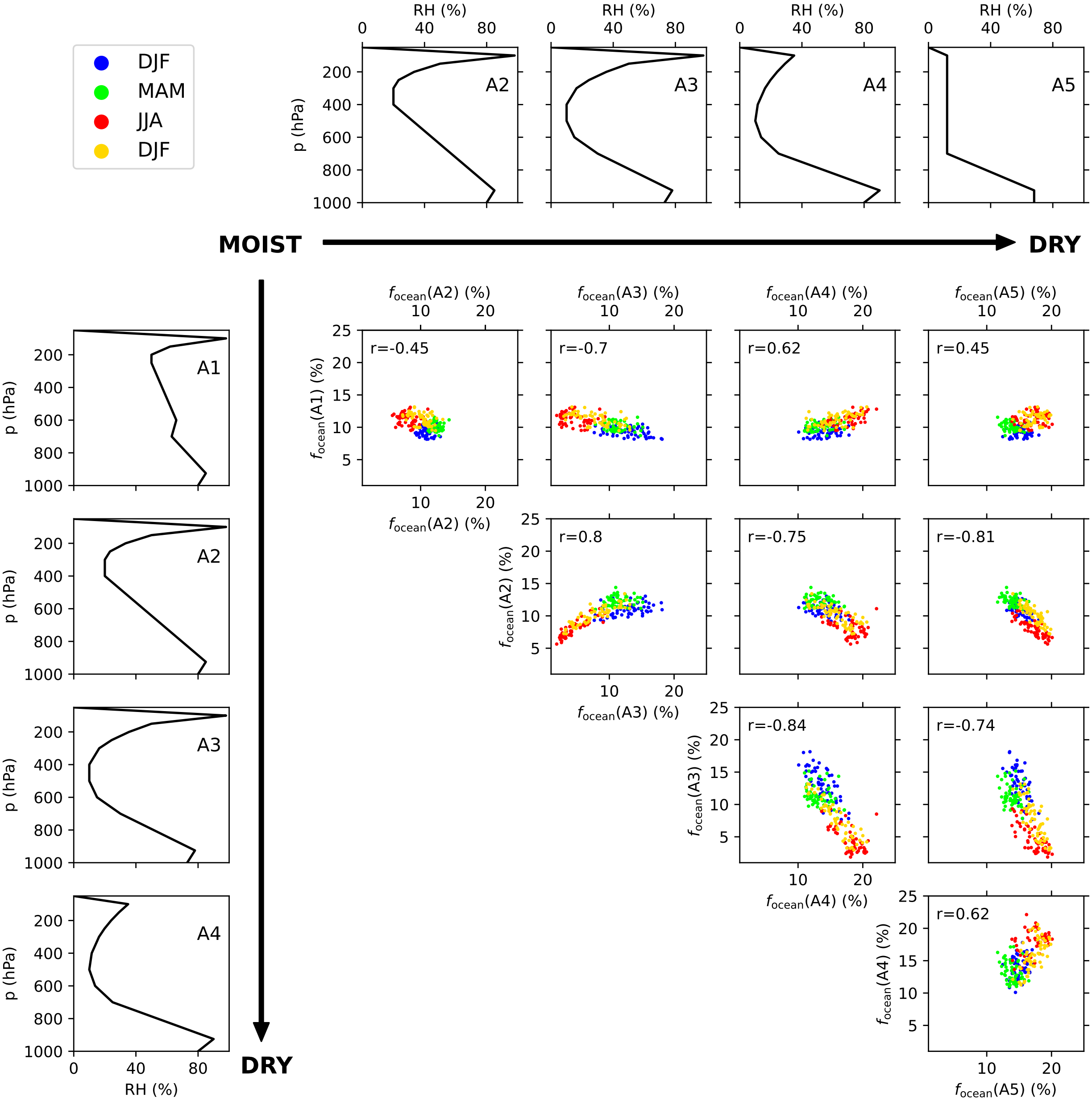

FIG. 7. Scatterplots of the monthly mean ocean fractions, f_{ocean}, of the tropics and subtropics dominating RH-profile classes A1–A5 (organized from moist to dry). Colors illustrate the different seasons (DJF: blue; MAM: green, JJA: red, SON: gold). Sketches on the left and top show idealized mean RH-profiles of the distinct classes.

While the magnitude of the seasonal f_{ocean}(A5) cycle is small (Fig. 3), it has a somewhat clear geographic distribution: a July–September maximum corresponds to increased occurrence in the southern subtropics, particularly in the Indian Ocean, during austral winter (Fig. 5).

The f_{ocean} of classes A6 and A8, in the mid- and high-latitudes have neither strong seasonal cycles nor strong spatial variation.

RH-profile class A7 occurs mostly in the Northern Hemisphere (Abraham and Goldblatt 2022), and most often in boreal summer, with a broad geographic distribution. There is a notable patch of elevated OP in the northwest Pacific during boreal winter. The uni-hemisphere boreal summer distribution and peculiar seasonality are curious, but explaining them is beyond the scope of this work (and beyond the scope of this data set as it could be an artifact of the cloud-clearing algorithms due to the often overcast conditions in those regions during DJF and the resulting low data availability in those regions). This result does speak to a historical curiosity: Profile A7 very closely resembles the RH-profile used by Manabe and Wetherald (1967) in the first work that correctly estimated Earth's climate sensitivity. Manabe and Wetherald (1967) drew heavily on Telegadas et al. (1954), whose model was specifically for the Northern Hemisphere.

b. Changes to RH-profile classes in a warming climate

As described above, structures of the different RH-profiles remain robust throughout the seasons; thus, spatial changes in humidity are accommodated via changes in OPs of RH classes. We now turn to analyze how robustly structures of RH-profiles are retained in annual means between 2003 and 2020. Furthermore, using decadal trend estimates (Sec. 2) we investigate how OP(k) and associated $f_{\text{ocean}}(k)$ evolve between those years. Both investigations indicate how global moisture distributions change in a warming climate.

In this dataset, the global mean SST decadal warming trend is about 0.42 K decade^{-1} (Table 2). This does not represent the actual global warming trend in the first two decades of the 21st century but simply the warming signal within this highly filtered dataset and spatially heterogeneously distributed data availability (cf. Sec. 2). Nonetheless, global and spatial warming signals can be used to infer from temporal trends linear warming responses to increasing SSTs. For instance, the global decadal trend of TPW within the data set is about 0.82 kg m^{-2} decade^{-1}, thus about 1.95 kg m^{-2} K^{-1} when divided by the SST trend (Table 2). Actual global SST trends through the last two decades are about 0.26-0.28 K decade^{-1} (Xu et al. 2021; Garcia-Soto et al. 2021). Over the same period the TPW trend was found to be about 0.54 kg m^{-2} decade^{-1} (Borger et al. 2022). Inferring from those estimates a linear global warming trend the measurements indicate a global

TABLE 2. Left: Annual and seasonal decadal trends of the all-sky globally averaged sea-surface temperatures (SST), outgoing longwave radiation (OLR), total precipitable water (TPW), as well as relative humidity (RH) at 925 and 700 hPa obtained from linear fits through seasonal stationary timeseries (seasonality removed according to Eq. 5). Right: Inferred linear trends of those state variables per SST increase of 1 K derived by dividing through ∂_t SST.

state variable	observed trend (unit decade^{-1})					observed trend (unit K^{-1})				
(unit)	Annual	DJF	MAM	JJA	SON	Annual	DJF	MAM	JJA	SON
SST (K)	0.42	0.27	0.48	0.55	0.38	—	–	–	–	–
OLR (W m^{-2})	0.70	0.55	0.84	0.79	0.60	1.67	2.04	1.75	1.44	1.58
TPW (kg m^{-2})	0.82	0.63	0.88	1.08	0.69	1.95	2.33	1.83	1.96	1.81
RH (925 hPa) (%)	2.16	2.03	2.98	2.1	1.52	5.14	7.52	6.21	3.82	4.00
RH (700 hPa) (%)	-0.70	-0.51	-1.22	-0.51	-0.56	-1.67	-1.89	-2.54	-0.93	-1.47

TPW trend of about 1.93–2.08 kg m^{-2} K^{-1}. Hence, our inferred trend estimates from a linear response to warming (from the filtered data set) agree with in-situ observations, other unfiltered satellite products, and reanalysis data.

Consistent with the general global warming trend the globally averaged OLR trend increases as well by about 1.7 W m^{-2} K^{-1}.

While the magnitudes of decadal trends are particular to this dataset (as described above), the spatial patterns of decadal trends in SST, OLR, and TPW are consistent with their most recent estimates from other satellite products (Figure 8). Ocean surfaces are warming; the spatial pattern of largest warming in the Northern and Northeast Pacific, weakest warming in the Central Pacific, and generally weak warming in the tropics and Southern East Pacific is consistent with other studies (cf. Fig. 1 in Xu et al. 2021; Garcia-Soto et al. 2021). Consistent with Xu et al. (2021) and Garcia-Soto et al. (2021) this dataset also exhibits the cooling of the North Atlantic and Southern Ocean around Antarctica (cf. Fig. 1 in Xu et al. 2021; Garcia-Soto et al. 2021), however, the weak cooling of the tropical Atlantic in this dataset does not agree with other studies. While this peculiarity is intriguing, it is beyond the scope of this paper to identify reasons for that inconsistency; inferred warming responses in those Central Atlantic regions should therefore be interpreted with caution.

The spatial patterns of OLR and TPW trends are anti-correlated: increases in TPW cause decreases in OLR (Fig. 8). In particular, over the East Pacific and Indian Ocean TPW trends are positive causing systematic OLR decreases; the reverse is found over the West Pacific. These spatial patterns are consistent with other satellite observations (cf. Whitburn et al. 2021; Borger

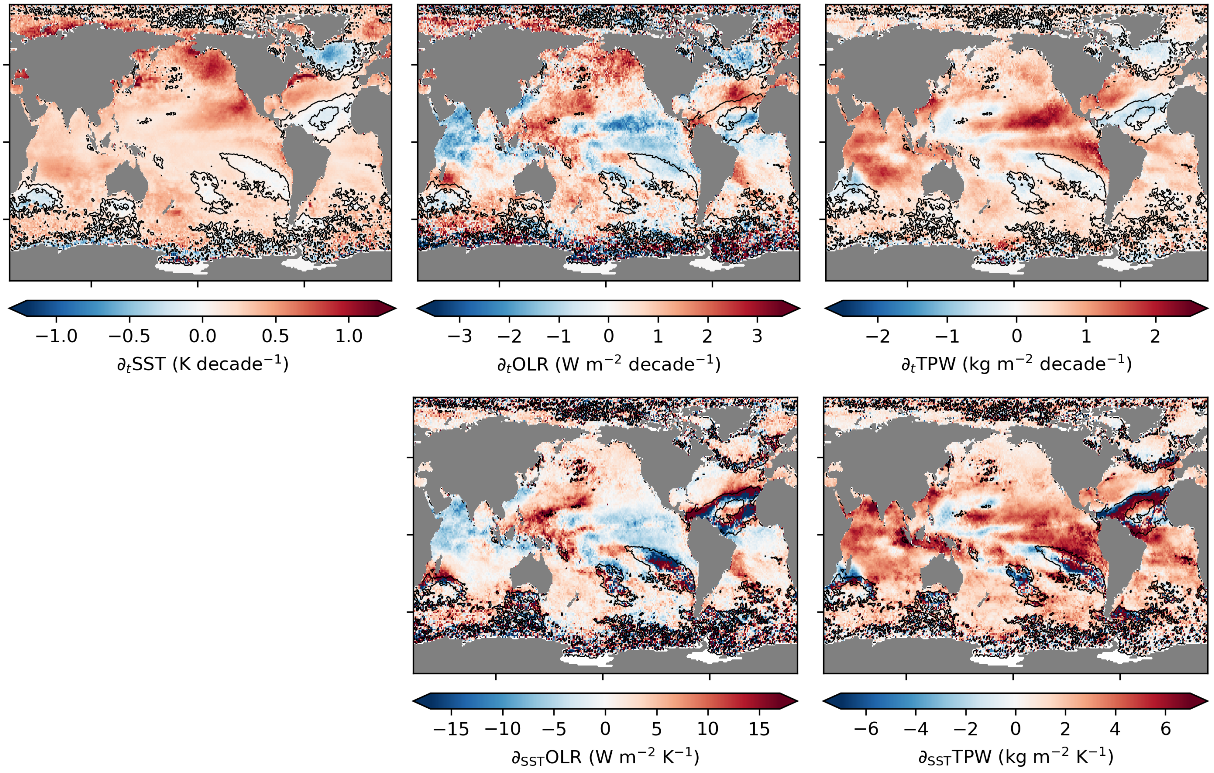

FIG. 8. Top from left: Decadal trends of SST, all-sky OLR, and TPW estimated from linear fits through seasonal stationary (seasonal cycle, Eq. 5, removed from timeseries) monthly means on a square degree uniform latitude-longitude grid between 2003 and 2020. Black contours illustrate areas where absolute SST trends are below 0.1 K decade^{-1}. The decadal trends (top row) estimated are particular to this highly-filtered AIRS data set and should not be directly compared to other studies. Bottom from left: Inferred linear OLR and TPW trends as a response to warming. The weak cooling in the Central Atlantic is inconsistent with other studies and inferred linear warming response estimates of all-sky OLR and TPW in that region should be interpreted with caution.

et al. 2022). The patterns in decadal trends of OLR resemble closely trends observed for the water vapour absorption band at about 7 μm in other satellite products (cf. Fig. 2d in Whitburn et al. 2021). Furthermore, except from the central Atlantic the estimated warming responses of both OLR and TPW are in good agreement with estimates in Whitburn et al. (2021) and Borger et al. (2022), respectively. Although inferred warming responses of OLR and TPW in the central Atlantic might be erroneous due to the estimated SST trends, the relative magnitudes of decadal trends are in agreement with Whitburn et al. (2021) and Borger et al. (2022).

TABLE 3. Left: Annual and seasonal decadal f_{ocean} trends of the 8 RH-profile classes obtained from linear fits to seasonally stationary timeseries (seasonal cycle, Eq. 5, removed). Right: Inferred linear trends of those quantities per global SST increase of 1 K.

RH-profile class	$\partial_t f_{\mathrm{ocean}}$ (% decade^{-1})					$\partial_{\mathrm{SST}} f_{\mathrm{ocean}}$ (% K^{-1})					$\partial_t \overline{\mathrm{SST}}$ (K dec^{-1})	$\partial_t \overline{\mathrm{TPW}}$ (kg m^{-2} dec^{-1})
season	Annual	DJF	MAM	JJA	SON	Annual	DJF	MAM	JJA	SON	Annual	Annual
A1	0.53	0.50	0.72	0.65	0.23	1.26	1.85	1.50	1.18	0.60	0.21	0.73
A2	0.61	0.46	0.44	1.02	0.54	1.45	1.70	0.92	1.85	1.42	0.31	0.67
A3	-0.46	-1.52	-0.40	0.24	-0.17	-1.10	-5.63	-0.83	0.44	-0.45	0.32	0.36
A4	1.92	1.83	2.67	1.74	1.44	4.57	6.78	5.56	3.16	3.79	0.25	0.40
A5	-1.06	-0.51	-1.12	-1.63	-0.99	-2.52	- 1.89	-2.33	-2.96	-2.61	0.39	0.36
A6	-0.06	-0.01	-0.25	-0.07	0.1	- 0.14	-0.03	-0.52	-0.13	0.26	0.21	0.27
A7	-0.79	-0.45	-1.14	-1.04	-0.52	-1.88	-1.67	-2.38	-1.89	-1.37	-0.14	0.16
A8	-0.69	-0.30	-0.92	-0.91	-0.63	-1.64	-1.11	-1.92	-1.65	-1.66	0.19	0.32

1) OCCURRENCE PROBABILITIES

Over the full 18 years of observations all RH-classes exhibit weak but continuous changes to their associated f_{ocean} both annually and seasonally (Figure 3; column 2). These changes are almost linear, particularly evident in the 10-year moving averages of the OPs (solid lines). The ocean fraction associated with both deep convection classes increases by about 1 % decade^{-1} (Table 3; $\partial_t f_{\mathrm{ocean}}(A1) + \partial_t f_{\mathrm{ocean}}(A2)$). The overall largest positive trends in f_{ocean} (about 2 % decade^{-1}) are found for class A4, indicating the increase in occurrences of RH-structures that are associated with low-level stratocumulus clouds. In general in this data set, all f_{ocean} of all extra-tropical RH-profile classes decrease.

The almost linear trends allow for inferring the f_{ocean} response to a globally warming climate (∂_{SST}) using the global SST trend (Table 2). Areas dominated by RH-profiles associated with strong and weak deep convection (A1 and A2) are then expected to increase by 1.26 % K^{-1} and 1.45 % K^{-1}, respectively. Ocean areas dominated by RH-profiles associated with low-level stratocumulus clouds, $f_{\mathrm{ocean}}(A4)$, are inferred to increase by about 4.57 % K^{-1}.

Geographically, RH-profiles associated with strong deep convection (A1) occur more frequently in the East Pacific, Indian Ocean, and the Southern Hemisphere tropical Atlantic, particularly in the regions of the ITCZ (Fig. 9); OP(A1) decreases are evident in the West Pacific, north of Australia and Indonesia. RH-profiles associated with weaker deep convection (A2) exhibit negative trends over regions of the ITCZ but positive trends around the ITCZ. This observation is consistent with the fact that the ITCZ becomes narrower and more intense within its core in a warming climate (Byrne and Schneider 2016; Byrne et al. 2018). More intense vertical motion in an intensified ITCZ supports increases in strong deep convection (associated with A1) which particularly over the colder East Pacific causes the substantial OP increase of A1 and consistently decreases in A2 (associated with weaker deep convection).

An intensifying ITCZ core causes increases in large-scale subsidence. Consistently, the OP increases of A1 and A2 are accompanied by OP decreases of A3 to be replaced by A4, particularly in the East Pacific, Indian Ocean, and Southern Atlantic. The same regions are more frequently populated by A4, the class associated with a drier free troposphere due to strong large-scale subsidence. In fact, both hemispheres outside the tropics experience large OP increases of A4 indicating conditions associated with low-level clouds.

Evidently, OPs of all remaining classes decrease in the extratropics. There are no particular regions associated with those decreases which is likely related to the fact that those regions are dynamically more variable.

2) RH-structures

The distinct RH-profile structures remain robust across all RH-profile classes between 2003 and 2020 (Fig. 10, left column). Evidently, RH-values below 850 hPa, atmospheric levels usually within the marine boundary layer, exhibit decadal trends of about 1.5-3 % decade^{-1} across all profiles between 2003 and 2020 (Fig. 10, middle column). Lowest marine boundary layer increases are found for the tropical classes (A1–A3) and the largest increase for A4 which naturally has large RH-values in the marine boundary layer. Between 850 hPa and 700 hPa RH-profiles we detect systematic decadal drying trends of about 1 % decade^{-1} in all classes. Above 700 hPa no systematic decadal changes to the vertical RH-profile structures are evident. This indicates that RH-values in the free troposphere remain approximately constant.

As SSTs in this dataset systematically increase (Figs. 4 and 8), the general signal of increasing RH in the marine boundary layer can be related to enhanced evaporation in a warming climate (e.g Díaz et al. 2019). The drying of the lower troposphere is likely related to the general warming of the atmosphere while absolute humidity within classes do not increase proportionally (Soden and Held 2006).

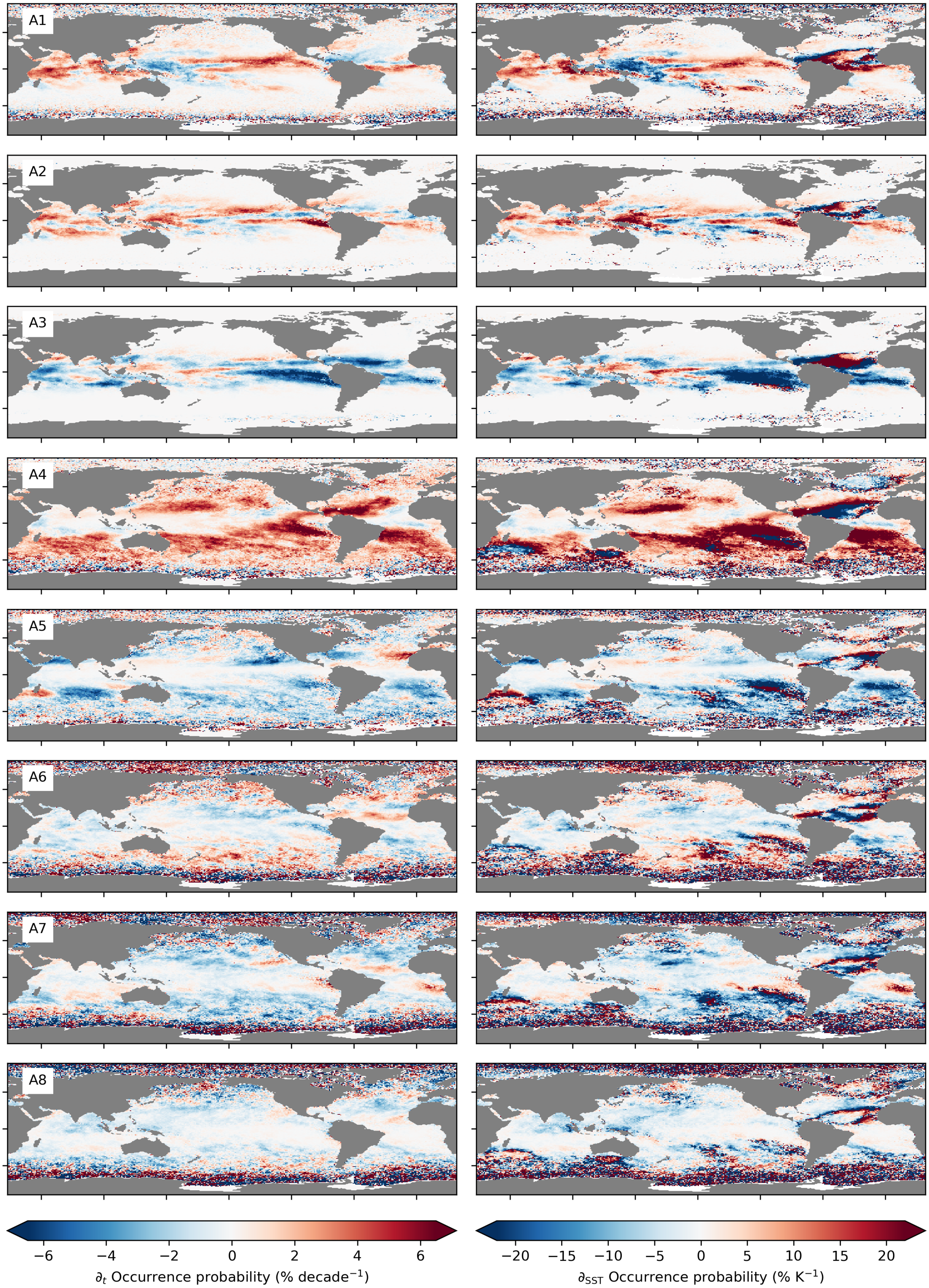

Accepted for publication in *Journal of the Atmospheric Sciences.* DOI 10.1175/JAS-D-22-0119.1.

FIG. 9. Left: Decadal OP trends of each RH-profile class estimated from linear fits through seasonal stationary (seasonal cycle, Eq. 5, removed from timeseries) monthly means on a square degree uniform latitude-longitude grid between 2003 and 2020. Right: Inferred linear OP trends as a response to warming.

Irrespective of distinct RH-classes, the systematic $\langle \mathrm{RH} \rangle$ increase in the marine boundary layer (below 850 hPa) and decrease around 700 hPa occur in both annual and seasonal means (Fig. 11; top row). While the $\langle \mathrm{RH} \rangle$ change at around 700 hPa is almost linear, at around 925 hPa changes occur mainly between about 2012 to 2017. Before and after those times $\langle \mathrm{RH} \rangle$ around 925 hPa remains relatively steady. The time of this change corresponds with the end of the warming hiatus in the global surface-temperatures (e.g. Easterling and Wehner 2009; Foster and Rahmstorf 2011; Trenberth and Fasullo 2013; England et al. 2014) caused by the Interdecadal Pacific Oscillation (Dai et al. 2015). While the initial increase in boundary layer moisture after 2012 is consistent with increasing SSTs after the warming hiatus, understanding the leveling off of the $\langle \mathrm{RH} \rangle$ timeseries after 2017 is an intriguing direction of future research.

The linear decadal trends of the $\langle \mathrm{RH} \rangle$ at 925 and 700 hPa are about 2.1 and -0.7 % decade^{-1}, respectively. Even though at 925 hPa we overestimate the actual trend due to the nonlinear behaviour discussed above, the observed $\langle \mathrm{RH} \rangle$ change at 925 hPa between 2012 and 2017 remains much larger than the expected 1 % from climate projections (e.g Sherwood et al. 2010). This result is consistent with findings by Borger et al. (2022) who also estimated the $\langle \mathrm{RH} \rangle$ increase in the boundary layer to be much larger than the predicted 1 % K^{-1}. Nonetheless, water vapour retrievals in this part of the atmosphere are also less accurate than in the free atmosphere and can cause anomalous trends (cf. Sec. 2).

Geographically, the increase in marine boundary layer RH is observed over all oceans with the exception of regions with westerly off-shore winds in the trade-wind regions (Fig.11). Even in areas where the observations suggest SST decrease or almost no warming (South-East Pacific, Central Atlantic; black contours in Fig.11) RH increases are comparable to regions with much larger SST warming. That all regions exhibit comparable RH increases in the marine boundary layer suggests that not only the underlying SST control the RH but also atmospheric dynamics which might be the reason for the non-linear decadal trends of $\langle \mathrm{RH} \rangle$ at 925 hPa. As most of the water vapour mass

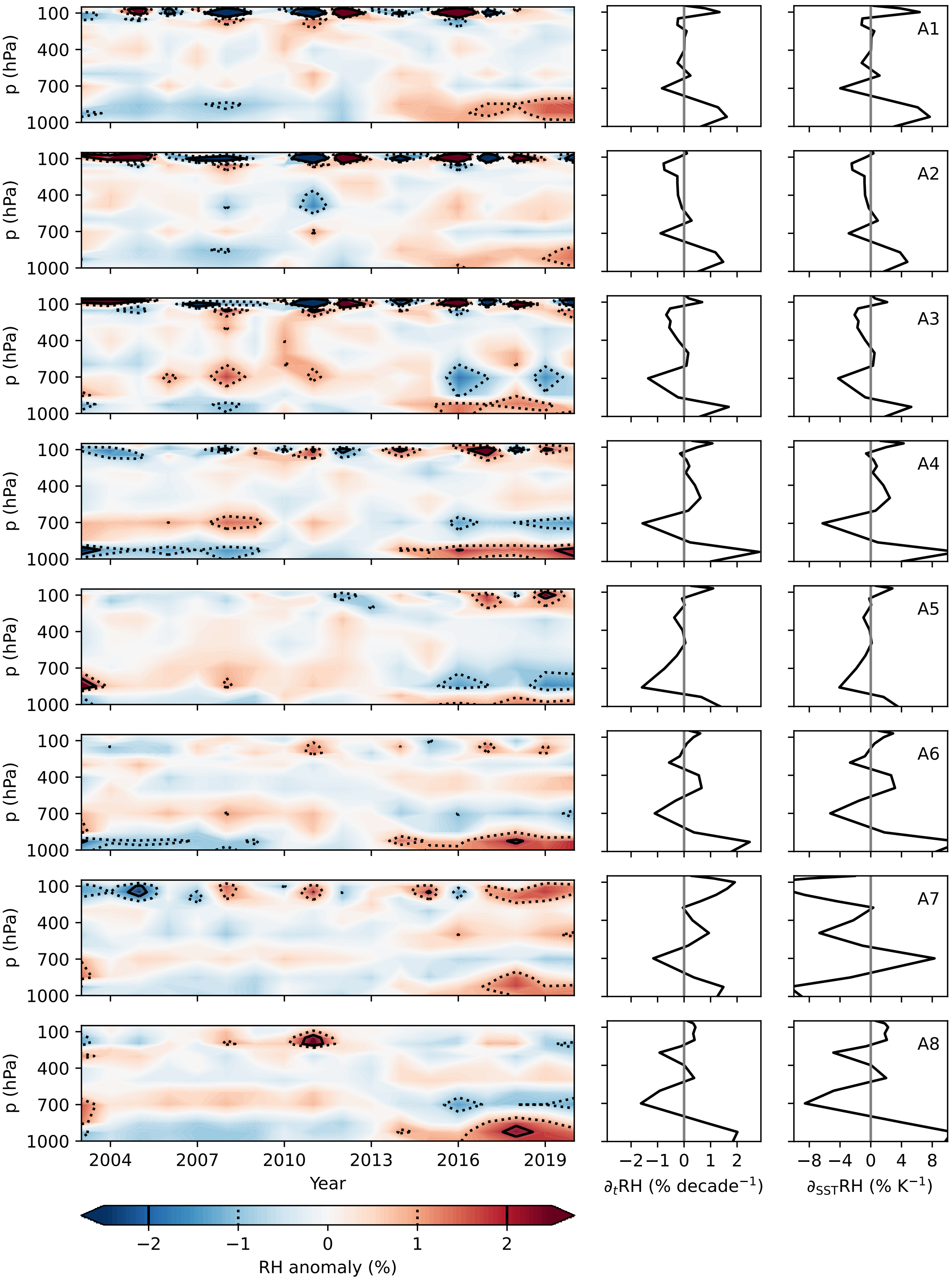

Accepted for publication in *Journal of the Atmospheric Sciences*. DOI 10.1175/JAS-D-22-0119.1.

FIG. 10. Left: Annual RH anomalies (colours) of the RH-profile classes against the climatological mean RH-profile structure between 2003 and 2020 (Fig 3; column 1, black lines). Within the difference plot values of ± 1 % and ± 2 % are illustrated with dotted and solid lines, respectively. Middle: Decadal trend (determined from linear fits to the anomalies) of RH-values at each level for all RH-profile classes. Right: Inferred linear warming response of RH values at each level within each RH-class using profile trends of the middle column and the RH-class specific observed SST trends (Table 3).

is found below 850 hPa (e.g. Borger et al. 2022), the general RH trends in the marine boundary layer causes the positive decadal trends in TPW in all classes (Table 3).

In contrast to RH trends at about 925 hPa, at 700 hPa the drying trends are spatially variable. In regions which are associated with increasing OP of A1 (East Pacific, Indian Ocean, Southern Hemisphere Central Atlantic) RH at 700 hPa increases by about 1 to 3 % decade^{-1}. Over all remaining areas RH decreases are of comparable magnitudes to the increases.

c. Inference of warming responses to globally averaged RH-profiles

In this data set, the estimated decadal trends of f_{ocean}, SSTs, and $\text{RH}(k,p)$ are almost linear, except for the RH(k, 925 hPa) which exhibit non-linear behaviour. Assuming the linear relationships are retained in a warming climate, we can infer the warming response of the globally-averaged vertical structure of RH over Earth's oceans. The $\langle \text{RH}(p) \rangle$ can be calculated from an area-weighted average over all $\overline{\text{RH}}(k,p)$:

$$\langle \text{RH}(p) \rangle = \sum_k f_{\text{ocean}}(k)\overline{\text{RH}}(k,p) \tag{6}$$

Using the inferred responses of $f_{\text{ocean}}(k)$ ($\partial_{\text{SST}} f_{\text{ocean}}(k)$; listed in Table 3) to warming and the climatological mean $\overline{f_{\text{ocean}}}(k)$ (Fig. 1) the projected change $f_{\text{ocean}}(k, \Delta\text{SST})$ to warming sea-surface temperatures, ΔSST, is

$$f_{\text{ocean}}(k, \Delta\text{SST}) = \overline{f_{\text{ocean}}}(k) + \partial_{\text{SST}} f_{\text{ocean}}(k)\ \Delta\text{SST}. \tag{7}$$

Applying further the warming $\partial_{\text{SST}}\text{RH}(k, p_{\text{lev}})$ (Figure 10; column 3) to the RH-values in each class the $\langle \text{RH(p)} \rangle$ is finally given by

Accepted for publication in *Journal of the Atmospheric Sciences*. DOI 10.1175/JAS-D-22-0119.1.

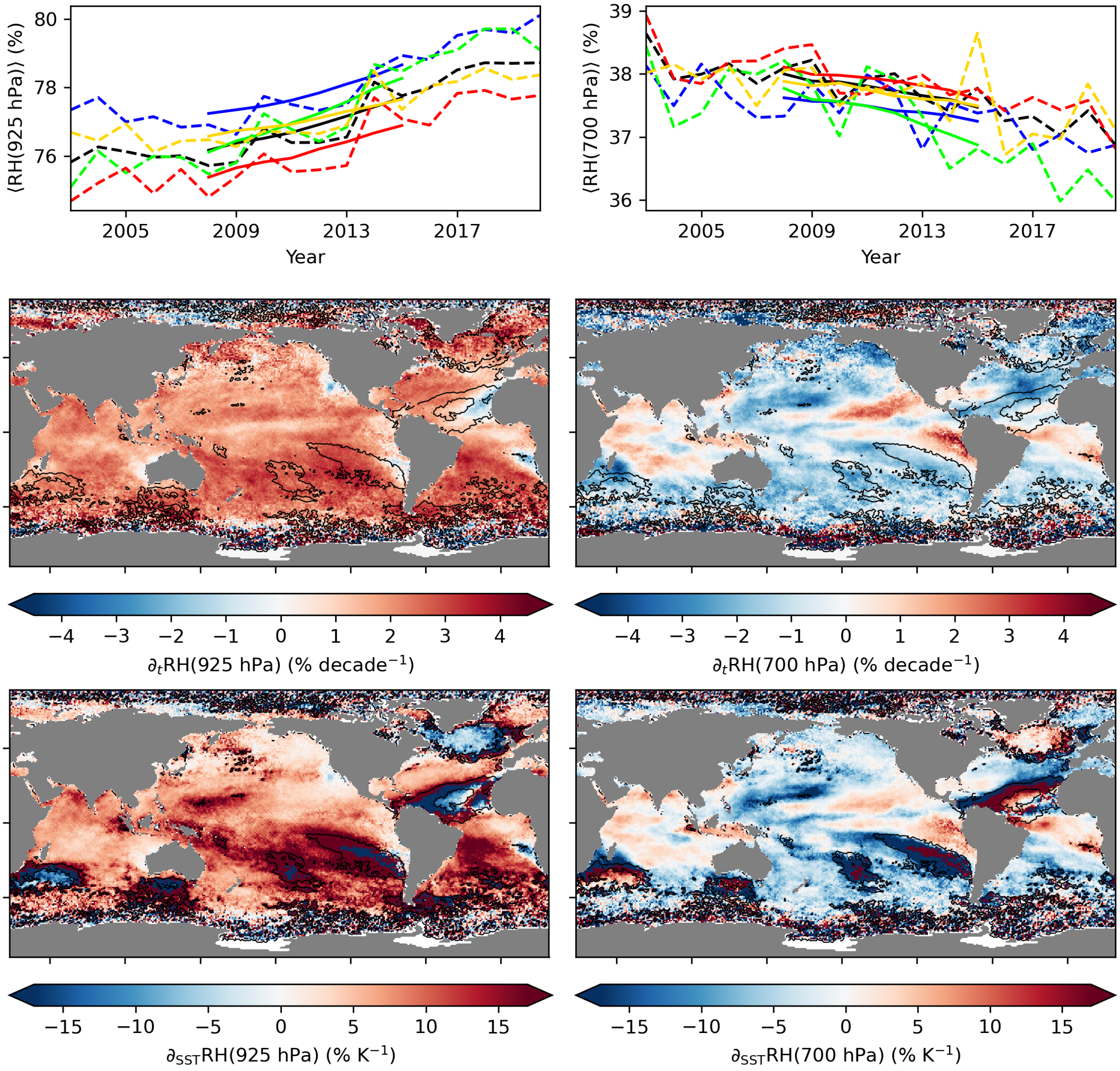

FIG. 11. Top row: Globally averaged timeseries of mean RH at 925 hPa (left) and 700 hPa (right) between 2003 and 2020 for the annual mean (black), DJF (blue), MAM (lime), JJA (red), and SON (orange). The annual means are illustrated with dotted lines and the 10-year moving averages by solid lines. Middle and bottom row: Spatially-resolved decadal trends and the inferred response to warming SST of 925 hPa (left) and 700 hPa (right) as in Fig. 8.

$$\langle \mathrm{RH}(p, \Delta\mathrm{SST}) \rangle = \sum_k f_{\mathrm{ocean}}(k, \Delta\mathrm{SST}) \left[\overline{\mathrm{RH}}(k, p) + \partial_{\mathrm{SST}} \mathrm{RH}(k, p)\ \Delta\mathrm{SST} \right]. \tag{8}$$

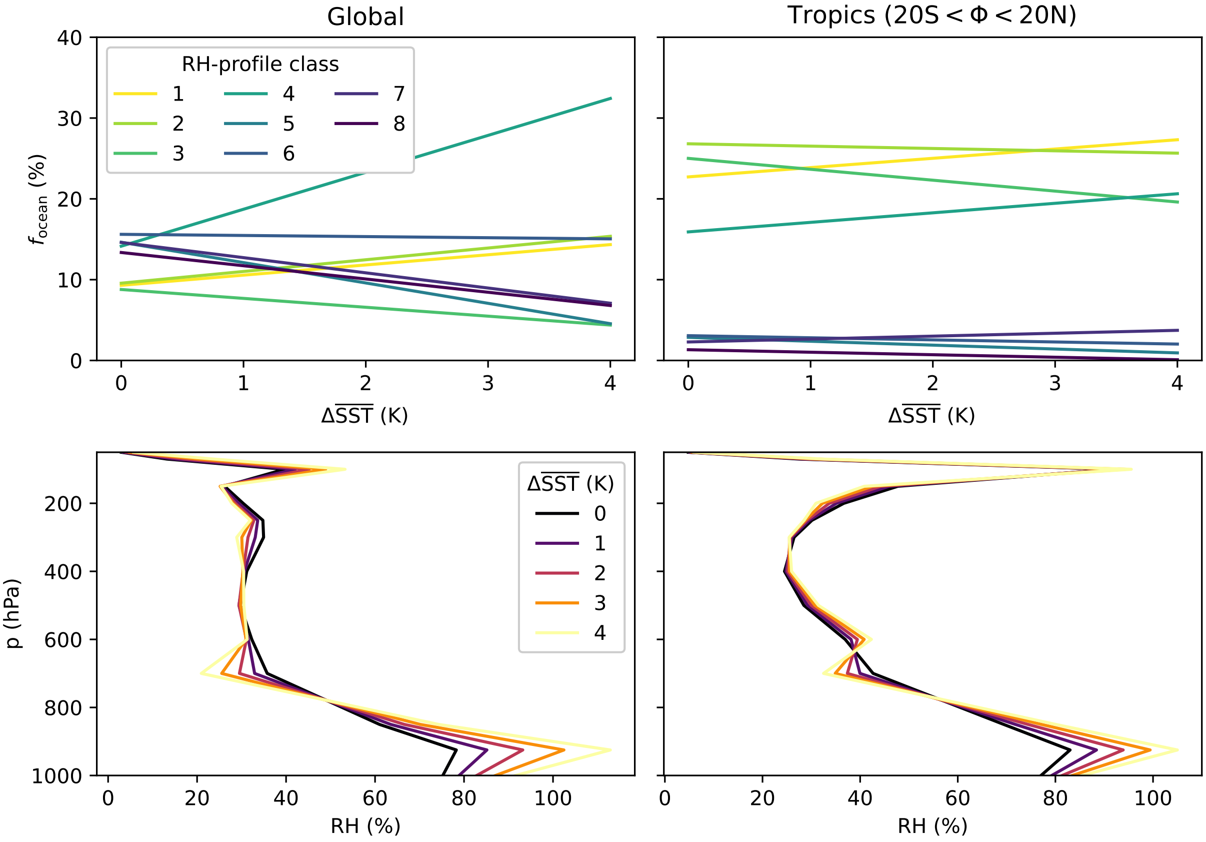

FIG. 12. Top: Linearly-projected response of the annual ocean fractions (f_{ocean}) dominated by each RH-profile class to global SST warming ($\Delta\overline{\text{SST}}$) for the entire global ocean (left) and the tropics (right). The response of f_{ocean} to warming is calculated following Eq. 7 using information of Fig. 1 and 3. Bottom: Linearly-projected response of global and tropical average RH-profiles for 4 different global and tropical SST warmings calculated following Eq.8 with information from Fig. 1 and 3 and the RH class specific vertical RH-response to SST warming (Fig. 10; column 3).

The inferred estimate of the warming responses of all $f_{\text{ocean}}(k)$ is illustrated in Fig. 12 (top left) exhibiting an increase in areas associated with RH-profile classes associated with deep convection (A1 and A2) and dry conditions in descending limbs with possibly low-level clouds (A4); f_{ocean} of remaining classes decrease.

Over the 18 years of observations, the $\langle \text{RH}(925\,\text{hPa}) \rangle$ consists of a marine boundary layer with RH around 80 %, followed by a linear decrease towards about 35 % $\langle \text{RH} \rangle$ at about 700 hPa (Fig. 12; bottom left, black line). Above 700 hPa the $\langle \text{RH}(p) \rangle$ remain constant up to the lower stratosphere.

The ⟨RH(p)⟩ exhibit only weak responses for $p < 925\,\mathrm{hPa}$ if all quantities discussed responded linearly to a warming climate. This result indicates that changes in $f_{\mathrm{ocean}}(k)$ must have compensating effects. The only evident warming response is observed in the marine boundary layer, however, as mentioned above, the assumption of a linear response is likely inaccurate for that atmospheric level. The result that $\langle \mathrm{RH}(p) \rangle$ change only weakly in a warming climate is consistent with future projections in climate models (e.g. Colman and Soden 2021; Soden and Held 2006; Sherwood et al. 2010; Laîné et al. 2014).

The result of almost preserved RH-profiles is not particular to the global average but also holds in other larger zonal bands such as the tropics (Fig 12; right panels). While the inferred estimates suggest that the global RH changes only weakly in a warming climate, local changes can be substantial. As in particular areas associated with deep convection and dry free atmospheres increase, the results suggest that regions with extreme moisture and dryness increase, thus either the frequency or persistence of extreme events can be enhanced. This result is consistent with recent observations and future projections of extreme precipitation (e.g., Myhre et al. 2019; Kirchmeier-Young and Zhang 2020; Tabari 2020; Chang et al. 2022) and drought events (e.g., Cowell and Urban 2010; Gamelin et al. 2022; Rakovec et al. 2022).

4. Conclusion

We have investigated how the classes of ‘primitive’ relative humidity (RH) profile structures identified by Abraham and Goldblatt (2022) from satellite data over Earth’s oceans vary seasonally, and decadally through 18 years of day- and night-time observations. As RH structures within each class are robust over the course of a year, seasonal water vapour redistributions manifest through local OP changes of RH-classes; or globally integrated via area changes over which on average each RH-profile class is dominant. All areas exhibit clear seasonal cycles with annual and semiannual harmonics. Interannual variability is weak and no phase shifts in seasonal cycles are observed.

Seasonally, changes to the occurrence of RH-profile classes compensate each other: areal increases in RH-profiles associated with deep convection give rise to the occurrence of drier profiles. We identify the ocean area of classes associated with deep convection to be closely correlated with that of remaining drier tropical classes through atmospheric dynamics: increases in the occurrences of class A1 (strong deep convection) causes occurrence decreases in class A3 (weaker

Accepted for publication in *Journal of the Atmospheric Sciences*. DOI 10.1175/JAS-D-22-0119.1.

large-scale subsidence) but increases in class A4 (stronger large-scale subsidence); an increase in the occurrence of weak deep convection (A2), on the other hand, causes increases (decreases) in the occurrence of A3 (A4). Only weak correlation in areal occurrence between classes A1 and A2 could be identified, consistent with the fact that their occurrence depend on the underlying sea-surface temperatures (SST) and not on atmospheric dynamics (cf. Abraham and Goldblatt 2022). Particularly in the tropics, seasonal occurrence maxima and minima of profiles associated with strong and weak deep convection (A1 and A2, respectively) coincide with average SST maxima and minima. The Indo-Pacific warmpool region and seas around Middle America experience substantial OP increases of A1 from boreal winter to boreal summer.

On the basis of seasonal stationary timeseries decadal trends of the global ocean area dominated by a particular class, RH profile structures, and SSTs are estimated. While our estimated decadal trends are particular to the highly-filtered data set, inferred trends to warming SSTs (derived by normalizing with the specific SST trends) assuming linearity are consistent with other observational and modelling studies.

The distinct mean RH-profile structures are found to be remarkably robust in the free troposphere across the years except from two atmospheric layers. In the marine boundary layer a global moistening trend of about $5\,\%\,\mathrm{K}^{-1}$ is estimated, however, it is also the only variable that exhibits nonlinear trends. Most of the RH increase in the marine boundary layer is observed between 2010 and 2016, the end of the warming hiatus and is therefore related to the overall SST increases and enhanced evaporation. Therefore, the linear decadal trends are most likely overestimated. Furthermore, that atmospheric layer has the lowest measurement accuracy int the dataset and a more detialed analysis has to be conducted. At about 700 hPa, on the other hand, we detect a systematic RH decrease of about $1.5\,\%\,\mathrm{K}^{-1}$ across all classes.

Inferring the responses of the areas dominated by each RH-profile class to a warming climate, the area associated with deep convection is projected to increase by about $2.5\,\%\,\mathrm{K}^{-1}$ almost equally divided between strong deep convection and weak deep convection. This increase is partially compensated by area increases of about $4.5\,\%\,\mathrm{K}^{-1}$ of class A4 which is associated with strong large-scale subsidence and likely low-level stratocumulus clouds. Geographically, increases and decreases of the class associated with strong deep convection (A1) are concentrated at the ITCZ

Accepted for publication in *Journal of the Atmospheric Sciences*. DOI 10.1175/JAS-D-22-0119.1.

centre and its edges, respectively. This result is consistent with a narrowing ITCZ with an intensified core in a warming climate (Byrne and Schneider 2016; Byrne et al. 2018).

The largest areal increase occurs for the class associated with strong large-scale subsidence, the class broadly consistent with low-level stratocumulus clouds (A4). While we infer that the features of A4 are broadly consistent with those cloud types (particularly as they are only observed for all-sky conditions, Abraham and Goldblatt 2022) a rigorous analysis of the exact cloud type distributions (including, for instance, optical thicknesses and cloud top heights) observed for that RH-profile class will be conducted. Similarly, a cloud-type climatology of the deep-convection classes would be useful. These are interesting directions of future research and could facilitate understanding connections between large-scale RH-distributions and cloud-type occurrences (e.g., Bony et al. 2015). This project also requires careful co-location of the AIRS L2 dataset with different satellite products such as MODIS L2.

Using estimated linear trends to global warming in RH-structures and occurrences of each RH-profile class, we find that globally and tropically averaged RH-profiles are remarkably robust to warming conditions. This finding is consistent with other studies (e.g. Colman and Soden 2021; Soden and Held 2006; Sherwood et al. 2010; Laîné et al. 2014). Our results, however, imply that moist and dry areas expand and compensate each other; hence, the distribution of moisture changes. This should cause intensifying moist and dry regions and is consistent with recent and projected increases in frequencies of extreme precipitation (e.g., Myhre et al. 2019; Kirchmeier-Young and Zhang 2020; Tabari 2020; Chang et al. 2022) and drought events (e.g., Cowell and Urban 2010; Gamelin et al. 2022; Rakovec et al. 2022).

With respect to climate sensitivity studies, the first order approximation of assuming globally a constant RH-structure (e.g Manabe and Wetherald 1967; Held and Soden 2000; Colman and Soden 2021) is consistent with our study if we assume the linear decadal trends estimated between 2003 and 2020 persist in the future. An intriguing direction of research would be to estimate climate sensitivity depending on the suite of RH-profile classes and their fractional contribution to the global radiation due to the close relationship to underlying SST. As shown in Abraham and Goldblatt (2022) deep convection classes exhibit nonlinear moisture feedbacks on the OLR, which might change the climate sensitivity due to the projected continuous areal increase of those classes (Pierrehumbert 1995).

Finally, while we accounted for seasonal variability in our trend estimates, the Pacific Ocean is governed by the interannual El-Niño Southern Osciallation (ENSO) which causes substantial changes to the Walker ciruclation and therefore changes to the updraft and downdraft regions. Furthermore, the Pacific and Indian Ocean are home to the Madden Julian Oscillation (MJO), an eastward propgating convection and cloud pattern. The influence of ENSO and MJO on the occurrence of the particular RH-profile classes will be discussed in a subsequent study.

Accepted for publication in *Journal of the Atmospheric Sciences*. DOI 10.1175/JAS-D-22-0119.1.

Acknowledgments. CA is supported by the floodplain mapping project of Environment and Climate Change Canada. Further financial support was provided by the Canadian Space Agency (grant 16SUASOMTR) and by the Natural Sciences and Engineering Research Council of Canada (NSERC; Discovery Grant RGPIN-2018-05929 and Research Tools and Equipment grant RTI-2020-00277). We thank two anonymous reviewers for their helpful comments and suggestions which improved the merit of the manuscript.

Data availability statement. The AIRS Version 7 Level 2 data are freely available via the Goddard Earth Sciences Data and Information Services Center (GES DISC, `https://disc.gsfc.nasa.gov`). The GES DISC provides additional information and documentation about the AIRS L2 products and other products of interest, as well as ordering and data sub-setting tools and services. We accessed the data on March 6 2021.

References

Abraham, C., and C. Goldblatt, 2022: A Satellite Climatology of Relative Humidity Profiles and Outgoing Thermal Radiation over Earth's Oceans. *Journal of the Atmospheric Sciences*, **79 (9)**, 2243–2265, https://doi.org/10.1175/JAS-D-21-0270.1, URL https://journals.ametsoc.org/view/journals/atsc/79/9/JAS-D-21-0270.1.xml.

Augustsson, T., and V. Ramanathan, 1977: A Radiative-Convective Model Study of the CO ¡sub¿2¡/sub¿ Climate Problem. *Journal of the Atmospheric Sciences*, **34 (3)**, 448–451, https://doi.org/10.1175/1520-0469(1977)034⟨0448:ARCMSO⟩2.0.CO;2, URL http://journals.ametsoc.org/doi/10.1175/1520-0469(1977)034⟨0448:ARCMSO⟩2.0.CO;2.

Aumann, H., and Coauthors, 2003: AIRS/AMSU/HSB on the aqua mission: design, science objectives, data products, and processing systems. *IEEE Transactions on Geoscience and Remote Sensing*, **41 (2)**, 253–264, https://doi.org/10.1109/TGRS.2002.808356, URL http://ieeexplore.ieee.org/document/1196043/.

Bony, S., and Coauthors, 2015: Clouds, circulation and climate sensitivity. *Nature Geoscience*, **8 (4)**, 261–268, https://doi.org/10.1038/ngeo2398, URL http://www.nature.com/articles/ngeo2398.

Borger, C., S. Beirle, and T. Wagner, 2022: Analysis of global trends of total column water vapour from multiple years of OMI observations. *Atmospheric Chemistry and Physics*, **22 (16)**, 10 603–10 621, https://doi.org/10.5194/acp-22-10603-2022, URL https://acp.copernicus.org/articles/22/10603/2022/.

Bourdin, S., L. Kluft, and B. Stevens, 2021: Dependence of Climate Sensitivity on the Given Distribution of Relative Humidity. *Geophysical Research Letters*, **48 (8)**, https://doi.org/10.1029/2021GL092462.

Byrne, M. P., A. G. Pendergrass, A. D. Rapp, and K. R. Wodzicki, 2018: Response of the Intertropical Convergence Zone to Climate Change: Location, Width, and Strength. *Current Climate Change Reports*, **4 (4)**, 355–370, https://doi.org/10.1007/s40641-018-0110-5, URL http://link.springer.com/10.1007/s40641-018-0110-5.

Byrne, M. P., and T. Schneider, 2016: Narrowing of the ITCZ in a warming climate: Physical mechanisms. *Geophysical Research Letters*, **43 (21)**, https://doi.org/10.1002/2016GL070396, URL https://onlinelibrary.wiley.com/doi/10.1002/2016GL070396.

Chaine, M. T., and Coauthors, 2006: Improving weather forecasting and providing new data on greenhouse gases. *Bulletin of the American Meteorological Society*, **87 (7)**, 911–926, https://doi.org/10.1175/BAMS-87-7-911, URL https://journals.ametsoc.org/doi/10.1175/BAMS-87-7-911.

Chang, M., B. Liu, B. Wang, C. Martinez-Villalobos, G. Ren, and T. Zhou, 2022: Understanding Future Increases in Precipitation Extremes in Global Land Monsoon Regions. *Journal of Climate*, **35 (6)**, 1839–1851, https://doi.org/10.1175/JCLI-D-21-0409.1, URL https://journals.ametsoc.org/view/journals/clim/35/6/JCLI-D-21-0409.1.xml.

Colman, R., and B. J. Soden, 2021: Water vapor and lapse rate feedbacks in the climate system. *Reviews of Modern Physics*, **93 (4)**, 045 002, https://doi.org/10.1103/RevModPhys.93.045002, URL https://link.aps.org/doi/10.1103/RevModPhys.93.045002.

Cowell, C. M., and M. A. Urban, 2010: The Changing Geography of the U.S. Water Budget: Twentieth-Century Patterns and Twenty-First-Century Projections. *Annals of the Association*

Accepted for publication in *Journal of the Atmospheric Sciences*. DOI 10.1175/JAS-D-22-0119.1.

of American Geographers, **100 (4)**, 740–754, https://doi.org/10.1080/00045608.2010.497117, URL http://www.tandfonline.com/doi/abs/10.1080/00045608.2010.497117.

Dacie, S., and Coauthors, 2019: A 1D RCE Study of Factors Affecting the Tropical Tropopause Layer and Surface Climate. *Journal of Climate*, **32 (20)**, 6769–6782, https://doi.org/10.1175/JCLI-D-18-0778.1, URL http://journals.ametsoc.org/doi/10.1175/JCLI-D-18-0778.1.

Dai, A., J. C. Fyfe, S.-P. Xie, and X. Dai, 2015: Decadal modulation of global surface temperature by internal climate variability. *Nature Climate Change*, **5 (6)**, 555–559, https://doi.org/10.1038/nclimate2605, URL http://www.nature.com/articles/nclimate2605.

Dewey, M., and C. Goldblatt, 2018: Evidence for Radiative-Convective Bistability in Tropical Atmospheres. *Geophysical Research Letters*, **45 (19)**, 673–10, https://doi.org/10.1029/2018GL078903, URL https://onlinelibrary.wiley.com/doi/abs/10.1029/2018GL078903.

Diao, M., L. Jumbam, J. Sheffield, E. F. Wood, and M. A. Zondlo, 2013: Validation of AIRS/AMSU-A water vapor and temperature data with in situ aircraft observations from the surface to UT/LS from 87°N-67°S. *Journal of Geophysical Research: Atmospheres*, **118 (12)**, 6816–6836, https://doi.org/10.1002/jgrd.50483, URL http://doi.wiley.com/10.1002/jgrd.50483.

Díaz, J. P., F. J. Expósito, J. C. Pérez, A. González, Y. Wang, L. Haimberger, and J. Wang, 2019: Long-Term Trends in Marine Boundary Layer Properties over the Atlantic Ocean. *Journal of Climate*, **32 (10)**, 2991–3004, https://doi.org/10.1175/JCLI-D-18-0219.1, URL https://journals.ametsoc.org/view/journals/clim/32/10/jcli-d-18-0219.1.xml.

Divakarla, M. G., C. D. Barnet, M. D. Goldberg, L. M. McMillin, E. Maddy, W. Wolf, L. Zhou, and X. Liu, 2006: Validation of Atmospheric Infrared Sounder temperature and water vapor retrievals with matched radiosonde measurements and forecasts. *Journal of Geophysical Research*, **111 (D9)**, D09S15, https://doi.org/10.1029/2005JD006116, URL http://doi.wiley.com/10.1029/2005JD006116.

Dunion, J. P., 2011: Rewriting the Climatology of the Tropical North Atlantic and Caribbean Sea Atmosphere. *Journal of Climate*, **24 (3)**, 893–908, https://doi.org/10.1175/2010JCLI3496.1, URL http://journals.ametsoc.org/doi/10.1175/2010JCLI3496.1.

Easterling, D. R., and M. F. Wehner, 2009: Is the climate warming or cooling? *Geophysical Research Letters*, **36 (8)**, L08 706, https://doi.org/10.1029/2009GL037810, URL http://doi.wiley.com/10.1029/2009GL037810.

England, M. H., and Coauthors, 2014: Recent intensification of wind-driven circulation in the Pacific and the ongoing warming hiatus. *Nature Climate Change*, **4 (3)**, 222–227, https://doi.org/10.1038/nclimate2106, URL http://www.nature.com/articles/nclimate2106.

Feltz, M. L., L. Borg, R. O. Knuteson, D. Tobin, H. Revercomb, and A. Gambacorta, 2017: Assessment of NOAA NUCAPS upper air temperature profiles using COSMIC GPS radio occultation and ARM radiosondes. *Journal of Geophysical Research: Atmospheres*, **122 (17)**, 9130–9153, https://doi.org/10.1002/2017JD026504, URL https://onlinelibrary.wiley.com/doi/abs/10.1002/2017JD026504.

Foster, G., and S. Rahmstorf, 2011: Global temperature evolution 1979–2010. *Environmental Research Letters*, **6 (4)**, 044 022, https://doi.org/10.1088/1748-9326/6/4/044022, URL https://iopscience.iop.org/article/10.1088/1748-9326/6/4/044022.

Galewsky, J., A. Sobel, and I. Held, 2005: Diagnosis of Subtropical Humidity Dynamics Using Tracers of Last Saturation. *Journal of the Atmospheric Sciences*, **62 (9)**, 3353–3367, https://doi.org/10.1175/JAS3533.1, URL https://journals.ametsoc.org/doi/10.1175/JAS3533.1.

Gamelin, B. L., J. Feinstein, J. Wang, J. Bessac, E. Yan, and V. R. Kotamarthi, 2022: Projected U.S. drought extremes through the twenty-first century with vapor pressure deficit. *Scientific Reports*, **12 (1)**, 8615, https://doi.org/10.1038/s41598-022-12516-7, URL https://www.nature.com/articles/s41598-022-12516-7.

Garcia-Soto, C., and Coauthors, 2021: An Overview of Ocean Climate Change Indicators: Sea Surface Temperature, Ocean Heat Content, Ocean pH, Dissolved Oxygen Concentration, Arctic Sea Ice Extent, Thickness and Volume, Sea Level and Strength of the AMOC (Atlantic Meridional Overturning Circulation). *Frontiers in Marine Science*, **8**, https://doi.org/10.3389/fmars.2021.642372, URL https://www.frontiersin.org/articles/10.3389/fmars.2021.642372/full.

Gettelman, A., W. D. Collins, E. J. Fetzer, A. Eldering, F. W. Irion, P. B. Duffy, and G. Bala, 2006: Climatology of Upper-Tropospheric Relative Humidity from the Atmospheric Infrared

Accepted for publication in *Journal of the Atmospheric Sciences*. DOI 10.1175/JAS-D-22-0119.1.

Sounder and Implications for Climate. *Journal of Climate*, **19 (23)**, 6104–6121, https://doi.org/10.1175/JCLI3956.1, URL http://journals.ametsoc.org/doi/10.1175/JCLI3956.1.

Gettelman, A., and Coauthors, 2004: Validation of Aqua satellite data in the upper troposphere and lower stratosphere with in situ aircraft instruments. *Geophysical Research Letters*, **31 (22)**, https://doi.org/10.1029/2004GL020730, URL http://doi.wiley.com/10.1029/2004GL020730.

Goldblatt, C., T. D. Robinson, K. J. Zahnle, and D. Crisp, 2013: Low simulated radiation limit for runaway greenhouse climates. *Nature Geoscience*, **6 (8)**, 661–667, https://doi.org/10.1038/ngeo1892, URL http://www.nature.com/articles/ngeo1892.

Held, I. M., and B. J. Soden, 2000: Water vapor feedback and global warming. *Annual Review of Energy and the Environment*, **25**, https://doi.org/10.1146/annurev.energy.25.1.441.

Jordan, C. L., 1958: MEAN SOUNDINGS FOR THE WEST INDIES AREA. *Journal of Meteorology*, **15 (1)**, 91–97, https://doi.org/10.1175/1520-0469(1958)015⟨0091:MSFTWI⟩2.0.CO;2, URL http://journals.ametsoc.org/doi/10.1175/1520-0469(1958)015⟨0091:MSFTWI⟩2.0.CO;2.

Kahn, B. H., and J. Teixeira, 2009: A Global Climatology of Temperature and Water Vapor Variance Scaling from the Atmospheric Infrared Sounder. *Journal of Climate*, **22 (20)**, 5558–5576, https://doi.org/10.1175/2009JCLI2934.1, URL http://journals.ametsoc.org/doi/10.1175/2009JCLI2934.1.

Kalmus, P., Sun Wong, and J. Teixeira, 2015: The Pacific Subtropical Cloud Transition: A MAGIC Assessment of AIRS and ECMWF Thermodynamic Structure. *IEEE Geoscience and Remote Sensing Letters*, **12 (7)**, 1586–1590, https://doi.org/10.1109/LGRS.2015.2413771, URL http://ieeexplore.ieee.org/document/7079476/.

Kirchmeier-Young, M. C., and X. Zhang, 2020: Human influence has intensified extreme precipitation in North America. *Proceedings of the National Academy of Sciences*, **117 (24)**, 13 308–13 313, https://doi.org/10.1073/pnas.1921628117, URL https://pnas.org/doi/full/10.1073/pnas.1921628117.

Kluft, L., S. Dacie, S. A. Buehler, H. Schmidt, and B. Stevens, 2019: Re-Examining the First Climate Models: Climate Sensitivity of a Modern Radiative–Convective Equilibrium Model.

Journal of Climate, **32 (23)**, 8111–8125, https://doi.org/10.1175/JCLI-D-18-0774.1, URL http://journals.ametsoc.org/doi/10.1175/JCLI-D-18-0774.1.

Korolev, A., and G. A. Isaac, 2006: Relative Humidity in Liquid, Mixed-Phase, and Ice Clouds. *Journal of the Atmospheric Sciences*, **63 (11)**, 2865–2880, https://doi.org/10.1175/JAS3784.1, URL https://journals.ametsoc.org/doi/10.1175/JAS3784.1.

Laîné, A., H. Nakamura, K. Nishii, and T. Miyasaka, 2014: A diagnostic study of future evaporation changes projected in CMIP5 climate models. *Climate Dynamics*, **42 (9-10)**, 2745–2761, https://doi.org/10.1007/s00382-014-2087-7, URL http://link.springer.com/10.1007/s00382-014-2087-7.

Liu, W. T., W. Tang, and P. P. Niiler, 1991: Humidity Profiles over the Ocean. *Journal of Climate*, **4 (10)**, 1023–1034, https://doi.org/10.1175/1520-0442(1991)004⟨1023:HPOTO⟩2.0.CO;2, URL http://journals.ametsoc.org/doi/10.1175/1520-0442(1991)004⟨1023:HPOTO⟩2.0.CO;2.

Maddy, E. S., and C. D. Barnet, 2008: Vertical Resolution Estimates in Version 5 of AIRS Operational Retrievals. *IEEE Transactions on Geoscience and Remote Sensing*, **46 (8)**, 2375–2384, https://doi.org/10.1109/TGRS.2008.917498, URL http://ieeexplore.ieee.org/document/4578827/.

Manabe, S., and R. T. Wetherald, 1967: Thermal Equilibrium of the Atmosphere with a Given Distribution of Relative Humidity. *Journal of the Atmospheric Sciences*, **24 (3)**, 241–259, https://doi.org/10.1175/1520-0469(1967)024⟨0241:TEOTAW⟩2.0.CO;2, URL http://journals.ametsoc.org/doi/10.1175/1520-0469(1967)024⟨0241:TEOTAW⟩2.0.CO;2.

Myhre, G., and Coauthors, 2019: Frequency of extreme precipitation increases extensively with event rareness under global warming. *Scientific Reports*, **9 (1)**, 16 063, https://doi.org/10.1038/s41598-019-52277-4, URL http://www.nature.com/articles/s41598-019-52277-4.

Nalli, N. R., and W. L. Smith, 2003: Retrieval of Ocean and Lake Surface Temperatures from Hyperspectral Radiance Observations. *Journal of Atmospheric and Oceanic Technology*, **20 (12)**, 1810–1825, https://doi.org/10.1175/1520-0426(2003)020⟨1810:ROOALS⟩2.0.CO;2, URL http://journals.ametsoc.org/doi/10.1175/1520-0426(2003)020⟨1810:ROOALS⟩2.0.CO;2.

Osei, M. A., L. K. Amekudzi, C. R. Ferguson, and S. K. Danuor, 2020: Inter-Comparison of AIRS Temperature and Relative Humidity Profiles with AMMA and DACCIWA Radiosonde Observations over West Africa. *Remote Sensing*, **12 (16)**, 2631, https://doi.org/10.3390/rs12162631, URL https://www.mdpi.com/2072-4292/12/16/2631.

Ovarlez, J., J.-F. Gayet, K. Gierens, J. Ström, H. Ovarlez, F. Auriol, R. Busen, and U. Schumann, 2002: Water vapour measurements inside cirrus clouds in Northern and Southern hemispheres during INCA. *Geophysical Research Letters*, **29 (16)**, 60–1, https://doi.org/10.1029/2001GL014440, URL http://doi.wiley.com/10.1029/2001GL014440.

Pierrehumbert, R. T., 1995: Thermostats, Radiator Fins, and the Local Runaway Greenhouse. *Journal of the Atmospheric Sciences*, **52 (10)**, 1784–1806, https://doi.org/10.1175/1520-0469(1995)052⟨1784:TRFATL⟩2.0.CO;2, URL http://journals.ametsoc.org/doi/10.1175/1520-0469(1995)052⟨1784:TRFATL⟩2.0.CO;2.

Pu, Z., and L. Zhang, 2010: Validation of Atmospheric Infrared Sounder temperature and moisture profiles over tropical oceans and their impact on numerical simulations of tropical cyclones. *Journal of Geophysical Research: Atmospheres*, **115 (D24)**, https://doi.org/10.1029/2010JD014258, URL http://doi.wiley.com/10.1029/2010JD014258.

Rakovec, O., L. Samaniego, V. Hari, Y. Markonis, V. Moravec, S. Thober, M. Hanel, and R. Kumar, 2022: The 2018–2020 Multi-Year Drought Sets a New Benchmark in Europe. *Earth's Future*, **10 (3)**, https://doi.org/10.1029/2021EF002394, URL https://onlinelibrary.wiley.com/doi/10.1029/2021EF002394.

Rennó, N. O., K. A. Emanuel, and P. H. Stone, 1994: Radiative-convective model with an explicit hydrologic cycle: 1. Formulation and sensitivity to model parameters. *Journal of Geophysical Research*, **99 (D7)**, 14 429, https://doi.org/10.1029/94JD00020, URL http://doi.wiley.com/10.1029/94JD00020.

Romps, D. M., 2014: An Analytical Model for Tropical Relative Humidity. *Journal of Climate*, **27 (19)**, 7432–7449, https://doi.org/10.1175/JCLI-D-14-00255.1, URL http://journals.ametsoc.org/doi/10.1175/JCLI-D-14-00255.1.

Ruzmaikin, A., H. H. Aumann, and E. M. Manning, 2014: Relative Humidity in the Troposphere with AIRS. *Journal of the Atmospheric Sciences*, **71 (7)**, 2516–2533, https://doi.org/10.1175/JAS-D-13-0363.1, URL https://journals.ametsoc.org/doi/10.1175/JAS-D-13-0363.1.

Sandor, B. J., E. J. Jensen, E. M. Stone, W. G. Read, J. W. Waters, and J. L. Mergenthaler, 2000: Upper tropospheric humidity and thin cirrus. *Geophysical Research Letters*, **27 (17)**, 2645–2648, https://doi.org/10.1029/1999GL011194, URL http://doi.wiley.com/10.1029/1999GL011194.

Satoh, M., and Y.-Y. Hayashi, 1992: Simple Cumulus Models in One-Dimensional Radiative Convective Equilibrium Problems. *Journal of the Atmospheric Sciences*, **49 (14)**, 1202–1220, https://doi.org/10.1175/1520-0469(1992)049⟨1202:SCMIOD⟩2.0.CO;2, URL http://journals.ametsoc.org/doi/10.1175/1520-0469(1992)049⟨1202:SCMIOD⟩2.0.CO;2.

Sherwood, S. C., R. Roca, T. M. Weckwerth, and N. G. Andronova, 2010: Tropospheric water vapor, convection, and climate. *Reviews of Geophysics*, **48 (2)**, RG2001, https://doi.org/10.1029/2009RG000301, URL http://doi.wiley.com/10.1029/2009RG000301.

Soden, B. J., and I. M. Held, 2006: An Assessment of Climate Feedbacks in Coupled Ocean–Atmosphere Models. *Journal of Climate*, **19 (14)**, 3354–3360, https://doi.org/10.1175/JCLI3799.1, URL http://journals.ametsoc.org/doi/10.1175/JCLI3799.1.

Stevens, B., and Coauthors, 2003: Dynamics and Chemistry of Marine Stratocumulus—DYCOMS-II. *Bulletin of the American Meteorological Society*, **84 (5)**, 579–594, https://doi.org/10.1175/BAMS-84-5-579, URL https://journals.ametsoc.org/doi/10.1175/BAMS-84-5-579.

Ström, J., and Coauthors, 2003: Cirrus cloud occurrence as function of ambient relative humidity: a comparison of observations obtained during the INCA experiment. *Atmospheric Chemistry and Physics*, **3 (5)**, 1807–1816, https://doi.org/10.5194/acp-3-1807-2003, URL https://acp.copernicus.org/articles/3/1807/2003/.

Susskind, J., C. Barnet, and J. Blaisdell, 2003: Retrieval of atmospheric and surface parameters from AIRS/AMSU/HSB data in the presence of clouds. *IEEE Transactions on Geoscience and Remote Sensing*, **41 (2)**, 390–409, https://doi.org/10.1109/TGRS.2002.808236, URL https://ieeexplore.ieee.org/document/1196056/.

Susskind, J., C. Barnet, J. Blaisdell, L. Iredell, F. Keita, L. Kouvaris, G. Molnar, and M. Chahine, 2006: Accuracy of geophysical parameters derived from Atmospheric Infrared Sounder/Advanced Microwave Sounding Unit as a function of fractional cloud cover. *Journal of Geophysical Research*, **111 (D9)**, D09S17, https://doi.org/10.1029/2005JD006272, URL http://doi.wiley.com/10.1029/2005JD006272.

Tabari, H., 2020: Climate change impact on flood and extreme precipitation increases with water availability. *Scientific Reports*, **10 (1)**, 13 768, https://doi.org/10.1038/s41598-020-70816-2, URL https://www.nature.com/articles/s41598-020-70816-2.

Takahashi, H., H. Su, and J. H. Jiang, 2016: Error analysis of upper tropospheric water vapor in CMIP5 models using "A-Train" satellite observations and reanalysis data. *Climate Dynamics*, **46 (9-10)**, 2787–2803, https://doi.org/10.1007/s00382-015-2732-9, URL http://link.springer.com/10.1007/s00382-015-2732-9.

Telegadas, K., J. London, A. F. C. R. C. U. G. R. Directorate, N. Y. U. D. of Meteorology, and Oceanography, 1954: *Physical Model of the Northern Hemisphere Troposphere for Winter and Summer*. Scientific report, New York University, Department of Meteorology and Oceanography, URL https://books.google.ca/books?id=YQYSHQAACAAJ.

Trenberth, K. E., and J. T. Fasullo, 2013: An apparent hiatus in global warming? *Earth's Future*, **1 (1)**, 19–32, https://doi.org/10.1002/2013EF000165, URL https://onlinelibrary.wiley.com/doi/10.1002/2013EF000165.

Trent, T., M. Schröder, and J. Remedios, 2019: GEWEX Water Vapor Assessment: Validation of AIRS Tropospheric Humidity Profiles With Characterized Radiosonde Soundings. *Journal of Geophysical Research: Atmospheres*, **124 (2)**, 886–906, https://doi.org/10.1029/2018JD028930, URL https://onlinelibrary.wiley.com/doi/10.1029/2018JD028930.

Whitburn, S., and Coauthors, 2021: Trends in spectrally resolved outgoing longwave radiation from 10 years of satellite measurements. *npj Climate and Atmospheric Science*, **4 (1)**, 48, https://doi.org/10.1038/s41612-021-00205-7, URL https://www.nature.com/articles/s41612-021-00205-7.

Accepted for publication in *Journal of the Atmospheric Sciences*. DOI 10.1175/JAS-D-22-0119.1.

Xu, Z., F. Ji, B. Liu, T. Feng, Y. Gao, Y. He, and F. Chang, 2021: Long-term evolution of global sea surface temperature trend. *International Journal of Climatology*, **41 (9)**, 4494–4508, https://doi.org/10.1002/joc.7082, URL https://onlinelibrary.wiley.com/doi/10.1002/joc.7082.

Accepted for publication in *Journal of the Atmospheric Sciences*. DOI 10.1175/JAS-D-22-0119.1.